Cross section measurements of proton capture reactions on Sr isotopes for astrophysics applications

S. Harissopulos,[*] E. Vagena, P. Dimitriou,[†] M. Axiotis, S. Galanopoulos,[‡] V. Foteinou,[§] and A. Lagoyannis
Institute of Nuclear and Particle Physics, NCSR "Demokritos", 153.10 Aghia Paraskevi, Athens, Greece

(Received 15 June 2020; accepted 21 July 2021; published 18 August 2021)

Background: Abundance calculations of a certain class of proton-rich isotopes, known as p nuclei, require knowledge of the cross sections of thousands of nuclear reactions entering a reaction network. As a result, the solution of the latter relies on the predictions of the Hauser-Feshbach (HF) theory and, hence, on the reliability of the models describing the nuclear parameters entering the HF calculations, notably the optical model potential (OMP), the nuclear level density (NLD) and the γ-ray strength function (γSF).
Purpose: The present work reports on a systematic study of proton capture reactions on Sr isotopes at energies relevant to the p process which is responsible for the production of the p nuclei at explosive stellar sites. The purpose of the work reported here is to perform a validity test of the different OMP, NLD, and γSF models through extensive and detailed comparisons between HF calculations and experimental cross section data. This test is necessary to understand the origin of discrepancies between the p-nuclei abundances observed in the solar system and those predicted by the different astrophysical models, known as p-process models, aiming at describing the nucleosynthesis of the p isotopes.
Method: Cross sections were determined from γ-angular distribution measurements and from angle-integrated γ spectra taken with the 4π γ-summing technique. Cross-section data and the resulting astrophysical S factors were compared with Hauser-Feshbach calculations obtained with the latest version 1.95 of the nuclear reaction code TALYS using combinations of global semi-microscopic and phenomenological models of optical potentials (OMPs), nuclear level densities (NLDs), and γ-ray strength functions (γSFs).
Results: Total cross sections as well as cross sections to the ground and metastable states were determined for the reactions ^{86}Sr$(p,\gamma)^{87}$Y, ^{87}Sr$(p,\gamma)^{88}$Y, and ^{88}Sr$(p,\gamma)^{89}$Y at incident proton-beam energies from 2.5 to 3.6, 2 to 5, and 1.5 to 5 MeV, respectively.
Conclusions: The experimental data reported in the present work are in very good agreement with the TALYS 1.95 calculations obtained with the default combination of OMP, NLD, and γSF models. This combination is based on purely phenomenological models. A semimicroscopic proton-nucleus optical model potential was optimized at low energies leading to an equally good agreement between experimental data and theoretical calculations based solely on combinations of fully semimicroscopic models of OMP, NLD, and γSF. Our results highlight the need for a continued effort on the systematic study of proton-capture reactions to reduce the range of uncertainties arising from global nuclear models for as wide a range of relevant nuclei as possible. In this regard, new (p,γ) data at the lowest possible energies below the opening of the neutron channel are of key importance to improve global proton-nucleus optical model potentials.

DOI: 10.1103/PhysRevC.104.025804

I. INTRODUCTION

Proton-nucleus and α-particle–nucleus optical model potentials (OMPs), nuclear level densities (NLDs), and γ-ray strength functions (γSFs) are among the major nuclear parameters which are of key importance in abundance calculations of a certain class of proton-rich isotopes, known as p nuclei. The latter lie between ^{74}Se and ^{196}Hg. According to the astrophysical models aiming at describing their nucleosynthetic mechanism termed the p process [1], p nuclei are produced in explosive stellar sites, such as Type II supernovae, under certain temperature conditions and isotopic composition.

The key role of OMPs, NLDs, and γSFs in p-process abundance calculations comes into play because the latter require solving a huge reaction network of more than 20 000 reactions involving almost 2000 stable or unstable isotopes lying between Ge and Bi (see, e.g., Fig. 4 of Ref. [2]). The reactions entering this network are neutron, proton, α-particle photodisintegrations, their competing capture reactions, as well as electron captures and β decays. The solution of this network means solving a system of a huge number of coupled differential equations containing primarily the decay rates of the unstable isotopes as well as the rates of the reactions involved. Hence, solving this network requires knowledge not

[*]Corresponding author: sharisop@inp.demokritos.gr
[†]Present address: Nuclear Data Section, International Atomic Energy Agency, Vienna 1400, Austria.
[‡]Present address: Archimedean Upper Conservatory, 12425 Sunset Dr., Miami, FL 33183, USA.
[§]Present address: DTL/RUBION, Ruhr-Universitat Bochum, 40781 Bochum, Germany.

TABLE I. Capture reactions investigated in the present work (1st column). The technique applied is given in the 2nd column. The corresponding incident beam energies E_p covered and typical beam currents i_p on target are given in the 3rd and 4th column, respectively. The material used to prepare the targets is listed in the 5th column, whereas the radial density (thickness) ξ of the corresponding target isotope and its enrichment are given in the 6th and 7th columns, respectively. The energy loss ΔE of a 3 MeV proton beam in the corresponding target was calculated with the code SRIM [12] and is listed in column 8.

Reaction	Technique	E_p (MeV)	i_p	Target material	ξ (μg/cm^2)	Enrichment (%)	ΔE (keV)
^{86}Sr$(p,\gamma)^{87}$Y	γ-angular distributions	2.5–3.6	5–10 μA	^{86}Sr CO$_3$	92 ± 7	96.89	5.6
^{86}Sr$(p,\gamma)^{88}$Y	4π γ-summing	2–3.5	5–12 nA	^{86}Sr CO$_3$	194 ± 16	96.89	12.3
^{87}Sr$(p,\gamma)^{88}$Y	γ-angular distributions	2–3.6	5–10 μA	^{87}Sr CO$_3$	73 ± 9	91.55	4.1
^{87}Sr$(p,\gamma)^{88}$Y	4π γ-summing	2.6–5	5–15 nA	^{87}Sr CO$_3$	96 ± 11	91.55	7.5
^{88}Sr$(p,\gamma)^{89}$Y	γ-angular distributions	2.5–3.6	5–10 μA	^{88}Sr$(NO_3)_2$	168 ± 12	99.84	9.5
^{88}Sr$(p,\gamma)^{89}$Y	4π γ-summing	2–5	4–12 nA	^{88}Sr$(NO_3)_2$	95 ± 7	99.84	15.9

only of a very high number of half-lives but also of a huge number of reaction cross sections from which the corresponding reaction rates are derived.

The huge number of the nuclear reactions entering the network makes the measurement of the cross section of every single reaction of the network an unrealistic task, also because the vast majority of the target nuclei can hardly be reached experimentally as they are unstable. As a result, the solution of the network relies necessarily on the predictions of the Hauser-Feshbach (HF) theory [3] that uses OMPs, NLDs, and γSFs as input parameters to calculate the cross sections. Although HF calculations are straightforward using well-established nuclear reaction codes [4–7], the resulting cross sections may vary significantly when using different model combinations of OMPs, NLDs, and γSFs. This was clearly demonstrated in two of our recent communications on (p,γ) reactions on Se [8] and Mo [9] isotopes.

Under these conditions, and on top of any p-process model deficiencies in reproducing the p-nuclei abundances observed in the solar system, it is necessary to perform a validity test of the models describing the nuclear properties entering the HF calculations.

Motivated by these scientific needs, we report here a systematic study of proton capture reactions on Sr isotopes at energies relevant to the p process. Results of this study were first reported for the total cross section of the ^{88}Sr$(p,\gamma)^{89}$Y reaction [10]. The present work complements the latter one with additional new (p,γ) cross sections. New results are also reported for ^{86}Sr and ^{87}Sr. All our experimental data are then compared with the corresponding HF calculations. Hereby, emphasis is given on testing the global character of existing proton-nucleus OMPs, NLDs, and γSFs.

II. SETUPS AND MEASUREMENTS

Experiments reported here were carried out either at the 4 MV single-stage Dynamitron accelerator of the previous Institut für Strahlenphysik (now closed) of the University of Stuttgart, Germany, or at the Dynamitron-Tandem-Laboratorium (DTL) of the Ruhr-Universität Bochum, Germany. In the former case, cross sections were determined by measuring γ-angular distributions at incident beam energies in the 2–3.6 MeV range, whereas in the latter one the 4π γ-summing technique [2,11] was employed using protons with energies from 2 to 5 MeV.

The properties of the Sr targets used are listed in table I. They were prepared by evaporating highly enriched isotopic material onto 0.2-mm-thick tantalum disks with a diameter of 4 cm. The areal densities ξ of the targets, often referred as to the "target thicknesses," were determined using the x-ray fluorescence (XRF) technique (see, e.g., [13]). The uncertainties in the thickness ξ given in Table I are the quadratic sum of systematic errors (7%) due to the XRF technique and the specific setup used, statistics (1–2%) and target homogeneities, which in the case of the ^{86}Sr and ^{88}Sr targets were between 3 to 4% and almost 10% for the ^{87}Sr target.

A. γ-angular distribution measurements

The γ-angular distributions were measured using the experimental setup described in detail in Refs. [2,10]. It consisted of four large-volume high-purity germanium detectors, all shielded with bismuth germanium oxide (BGO) crystals for Compton background suppression. Three of them had a relative efficiency of $\approx$100%, whereas the remaining one had $\approx$76%. The detectors were placed on a motor-driven table that could rotate. This way, γ-singles spectra were measured for the ^{86}Sr$(p,\gamma)^{87}$Y, ^{87}Sr$(p,\gamma)^{88}$Y, and ^{88}Sr$(p,\gamma)^{89}$Y reactions at eight angles with respect to the beam direction. At each beam energy, additional spectra were taken at each one of the eight angles with the proton beam impinging on a blank backing to check for possible yield contributions from reactions occurring in the backing material.

The absolute efficiency of the detector setup was determined at all eight angles as described in [10]. In addition, coincidence summing effects were checked following the procedure described in Ref. [14]. For this purpose, a ^{57}Co radioactive source was used in addition to ^{137}Cs and ^{60}Co sources. As expected, this effect was found to be negligible ($\leqslant$1%) as the distances of the detectors from the target were sufficiently long, i.e., between 10 and 20 cm. During the measurements, the current of the proton beam on the targets varied from 5 to 10 μA. The beam spot had a diameter of $\approx$4 mm.

Typical γ-singles spectra of the (p,γ) reactions on ^{86}Sr and ^{87}Sr, both taken with the Ge detector placed at 90° to

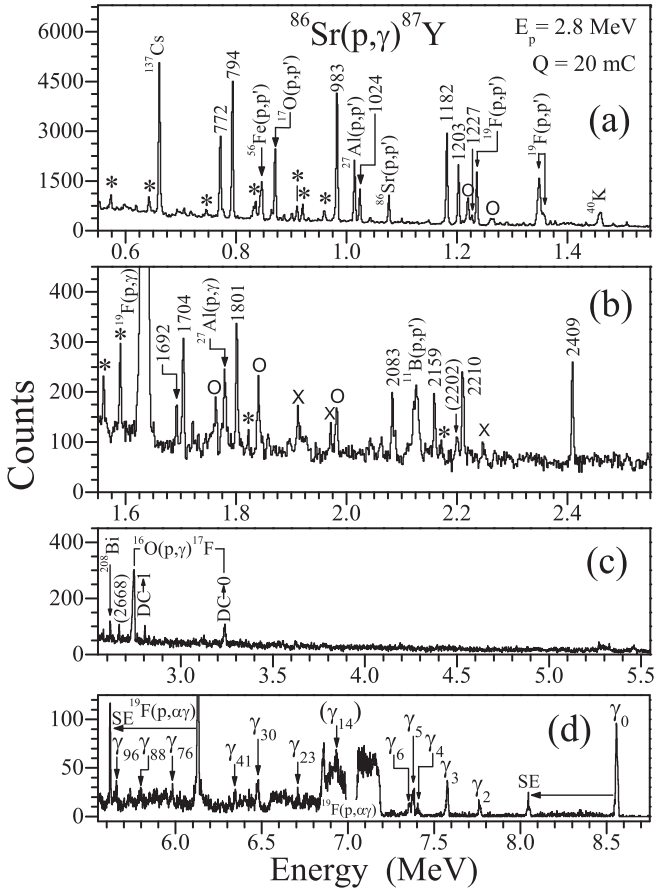

FIG. 1. Typical γ-singles spectrum measured at $E_p = 2.8$ MeV for the ^{86}Sr$(p,\gamma)^{87}$Y reaction with the Ge detector placed at 90° with respect to the beam axis. The accumulated beam charge Q was 20 mC. The γ transitions contained in the spectrum are explained in the text.

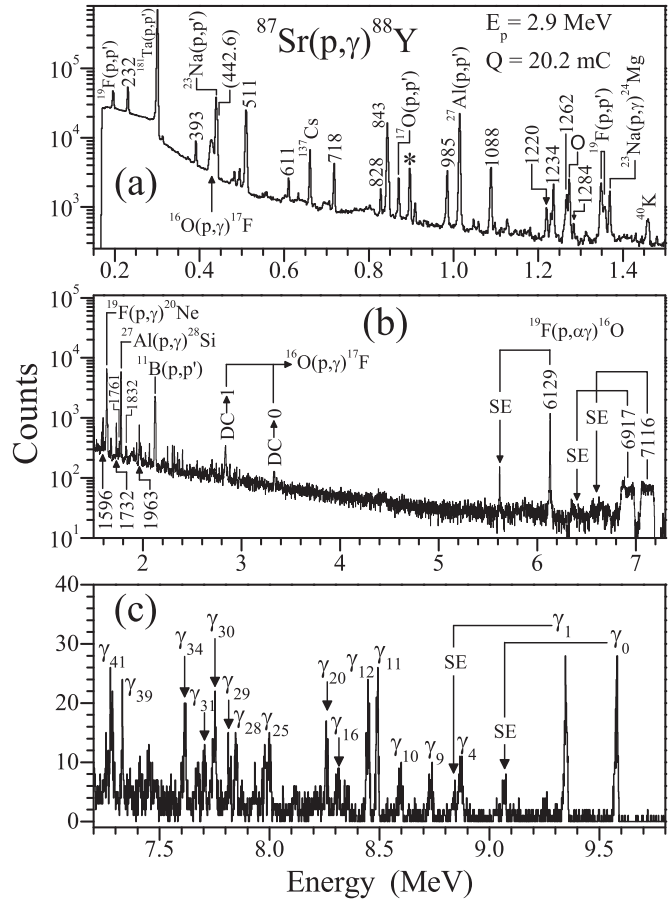

FIG. 2. Same as in Fig. 1 but for the ^{87}Sr$(p,\gamma)^{88}$Y measured at $E_p = 2.9$ MeV with $Q = 20.2$ mC. The γ transitions contained in the spectrum are explained in the text.

the beam axis, are shown in Figs. 1 and 2, respectively. The corresponding proton-beam energies were 2.8 and 2.9 MeV. For the ^{88}Sr$(p,\gamma)^{89}$Y reaction, a typical γ singles spectrum measured at 3 MeV at an angle of 90° with respect to the beam axis was already reported in [10].

In both spectra shown in Figs. 1 and 2, the *primary*γ transitions, i.e., γ rays deexciting the *entry* state of the produced compound nuclei ^{87}Y and ^{88}Y, respectively, are labeled as γ_i. The integer index i indicates the accession number of the populated excited state of the corresponding compound nucleus according to the level listing of the IAEA's Live Chart compilation [15]. The primaries observed in the case of ^{86}Sr$(p,\gamma)^{87}$Y are depicted in panel (d) of Fig. 1, whereas those detected from the ^{87}Sr$(p,\gamma)^{88}$Y reaction are shown in panel (c) of Fig. 2. In some cases, single escape peaks have also been observed. These are marked with SE. As both figures show, we were able to observe numerous primary γ rays, notably up to the 96th and 41st excited discrete levels of ^{87}Y and ^{88}Y, respectively. This was possible due to the high efficiency of the setup used.

Ideally, the total cross section could be obtained from the intensities of the primary transitions alone. However, we chose not to apply this type of analysis, not only to overcome problems in the data analysis due to the proton decay of unbound states after compound nucleus formation but also to avoid systematic errors arising from uncertainties in the level schemes—often encountered at high excitation energies—and the very weak intensities of primary γ lines that populate high-lying discrete levels. Hence, our data analysis of the γ-angular distribution measurements was based on the absolute intensities of the primary γ_0 line and those of the *secondary* γ transitions feeding the relevant ground states. As discussed in the next section, for the ^{86}Sr$(p,\gamma)^{87}$Y reaction, it was necessary to take into account the absolute intensities of the *secondary* γ transitions populating the first excited metastable state of ^{87}Y having an excitation energy $E_X = 381$ keV, since its half-life is $T_{1/2} = 13.37$ h and therefore the γ-ray depopulating this level could not be measured in-beam. In Figs. 1 and 2, the peaks of the secondary γ transitions taken into account to obtain the cross sections of interest are labeled with numbers indicating the corresponding photon energies in keV units. Moreover, peaks marked with an asterisk (*) correspond to secondary γ transitions feeding discrete states other than the ground states of ^{87}Y and ^{88}Y and, in the case of ^{86}Sr$(p,\gamma)^{87}$Y, other than the metastable state of ^{87}Y. Peaks marked with a circle are background γ rays observed in a

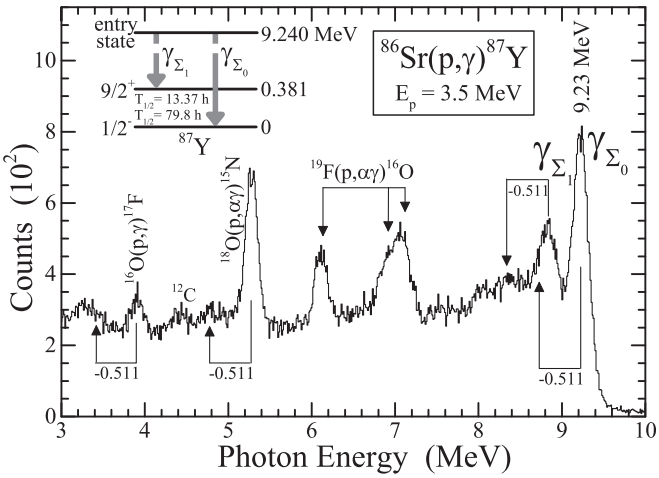

FIG. 3. High-energy part of the angle integrated γ spectrum measured for the ^{86}Sr$(p,\gamma)^{87}$Y reaction at a proton beam energy $E_p = 3.5$ MeV (see also text for details).

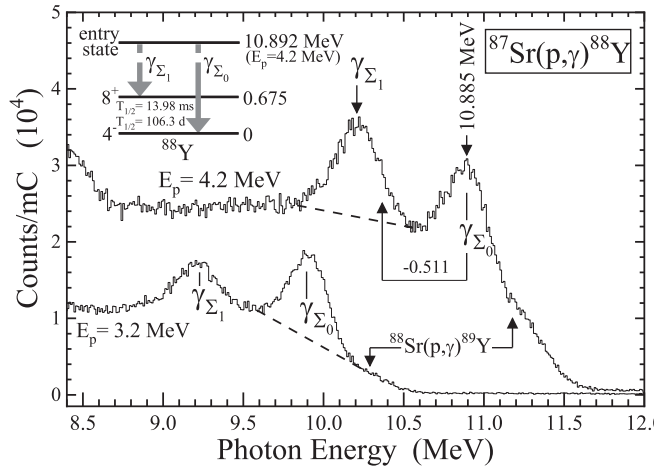

FIG. 4. High-energy part of the angle integrated γ spectra measured for the ^{87}Sr$(p,\gamma)^{88}$Y reaction at proton beam energies 4.2 and 3.2 MeV. The two dashed lines indicate typical linear interpolations for the subtraction of the background below the corresponding peaks (see also text for details).

series of (p,γ) reactions we have investigated previously. Only γ lines labeled with X are of unknown origin.

Both Figs. 1 and 2 contain also a peak labeled with ^{137}Cs, which is the 662-keV γ transition of a ^{137}Cs radioactive source that was used as "clock" during the measurements to check the dead time. It is worth noting that the spectra plotted in Figs. 1 and 2 include peaks resulting from the proton-induced reactions on ^{181}Ta, ^{56}Fe, ^{23}Na, ^{27}Al ^{19}F, ^{17}O, ^{16}O, and ^{11}B. All aforementioned reactions are due to the presence of elements either in the target (O) or the backing material (Ta, Na, F, B) or in mechanical parts of the whole setup.

B. Measurements with the 4π γ-summing method

The setup employed to measure angle-integrated γ rays emitted from all three aforementioned (p,γ) reactions using the 4π γ-summing technique is described in detail in Refs. [2,11]. This technique is based on the use of a large-volume NaI(Tl) detector covering a solid angle of almost 4π for photons emitted by a target placed at its center. The working principle of such a detector relies on its long time response and its large volume. The latter enables it to fully absorb a photon, whereas the former renders the photomultipliers unable to distinguish between different photons emitted within a time interval smaller than the decay time of the crystal, which is typically $\gtrsim$300 ns. As a result, the corresponding photons are recognized as one photon having an energy equal to the sum of their individual energies.

The main advantage of the 4π γ-summing technique is that, instead of measuring at least five γ spectra to obtain a γ-angular distribution at each beam energy and further analyzing numerous γ transitions, one needs to acquire only one spectrum and analyze only one γ peak, the so-called sum peak. Angle-integrated γ spectra measured with the 4π γ-summing method for ^{86}Sr$(p,\gamma)^{87}$Y and ^{87}Sr$(p,\gamma)^{88}$Y are shown in Figs. 3 and 4, respectively. For the ^{88}Sr$(p,\gamma)^{89}$Y reaction, a typical angle-integrated γ spectrum measured taken at 3.6 MeV is given in [11].

Figure 4 depicts the angle-integrated γ transitions measured with the 4π γ-summing technique at $E_p = 3.5$ MeV and with the proton beam impinging on a $^{86}SrCO_3$ target. As expected, the $(p,\alpha\gamma)$ reaction on ^{19}F, which is contained in the backing, and the (p,γ) reactions on ^{16}O and ^{18}O are also included in the spectra. Single-escape peaks visible in Fig. 3 are indicated with arrows (-0.511). The peak at $\approx$4.4 MeV corresponds to the first excited state of ^{12}C that is expected to produced by the (p,γ) reaction in ^{11}B that is contained in the backing material, as mentioned above.

The strong peak at 9.23 MeV shown in Fig. 3 is the sum peak γ_{Σ_0} of the ^{86}Sr$(p,\gamma)^{87}$Y reaction. This peak is the result of summing all γ transitions depopulating the entry state and cascading down to the ground state of ^{87}Y, including the γ_0 transition that was explained above. At an energy of 8.85 MeV, one observes a second sum peak (γ_{Σ_1}) resulting from the sum of all γ transitions depopulating the entry state and cascading down to the first excited (metastable) state of ^{87}Y, at $E_X = 381$ keV, as indicated in the inset of Fig. 3.

The presence of two sum peaks in the spectrum plotted in Fig. 3 is obvious since the half-life of the metastable state is 13.37 h, i.e., by far longer than the decay time of the NaI crystal ($\approx$300 ns), within which different photons are not distinguishable as discussed above. Similarly, the angle-integrated γ rays emitted by the ^{87}Sr$(p,\gamma)^{88}$Y reaction result in two different sum peaks, as shown in Fig. 4 for two different γ spectra measured at 4.2 and 3.2 MeV. These are expected because ^{88}Y has a metastable state with $T_{1/2} = 13.98$ ms, as shown in the inset of Fig. 4. Due to the much higher cross section of ^{88}Sr$(p,\gamma)^{89}$Y its sum peak is also visible on the right side of the sum peak of the ^{87}Sr$(p,\gamma)^{88}$Y reaction. Cases where more than one sum peaks appear in spectra taken with the 4π γ-summing method are discussed in more detail in [16].

III. DATA ANALYSIS AND RESULTS

As described in detail in [2], the total reaction cross section σ_{T} is derived from the total reaction yield Y_T:

$$\sigma_T = \frac{A}{N_A}\frac{Y_T}{\xi}, \tag{1}$$

where A is the atomic weight in amu of the target used, N_A is the Avogadro number, and ξ is the target "thickness" (radial density). In a (p,γ) reaction, the total reaction yield Y_T is the absolute number of photons emitted by the reaction per impinging proton.

In the case of γ-angular distribution measurements, the total yield Y_T is derived at each beam energy from the absolute intensities A_0 of the angular distributions of all the N γ transitions feeding the ground state of the produced compound nucleus, i.e.,

$$Y_T = \sum_i^N A_0^i. \tag{2}$$

If the excitation spectrum of the latter nucleus contains a long-lived metastable state which is deexcited via an $E0$ transition or has a half-life much longer than the measurement time, then Eq. (2) has to be applied twice, i.e., not only for the N γ transitions feeding the ground state but also for those (say, M in number) that populate the metastable state. In such a case, Y_T is derived as

$$Y_T = Y_g + Y_m = \sum_i^N A_0^i + \sum_j^M A_0^j. \tag{3}$$

If more metastable states exist at higher energies that do not feed into the ground or other metastable states, then Eq. (3) has to be modified accordingly.

From a comprehensive analysis of the γ spectra measured in the present work to obtain the γ-angular distributions of interest, we were able to conclude on all N and $M\gamma$ transitions feeding, respectively, the ground and metastable states of interest. These are given in the level schemes of the produced compound nuclei ^{87}Y and ^{88}Y that are shown in Figs. 5 and 6, respectively. According to the former figure, there are 11 γ transitions feeding the ground state of ^{87}Y and seven more γ lines populating its first excited $9/2^+$ metastable state, whereas for ^{88}Y it was found that its ground state is populated by 14 γ rays, as shown in Fig. 6.

In the case of ^{87}Sr$(p,\gamma)^{88}$Y, the total reaction yield Y was extracted from the absolute intensities A_0 of all 14 γ transitions populating the ground state of ^{88}Y, whereas in the case of ^{86}Sr$(p,\gamma)^{87}$Y it was necessary to take into account not only the 11 γ rays feeding the $1/2^-$ ground state of ^{87}Y but also the seven γ transitions populating its $9/2^+$ metastable state, which has a half-life $T_{1/2} = 13.37$ h. As a result, the total cross section σ_T of the latter reaction was deduced as the sum of the cross sections σ_g for the production of ^{87}Y in its ground state and σ_m for its production in its metastable state.

The ground state of ^{89}Y produced via the ^{88}Sr(p,γ) reaction is populated by 12 γ transitions and the σ_T of this reaction was determined similarly, as we reported in [10]. It is worth noting that the ^{89}Y nucleus has also a $9/2^+$ metastable state

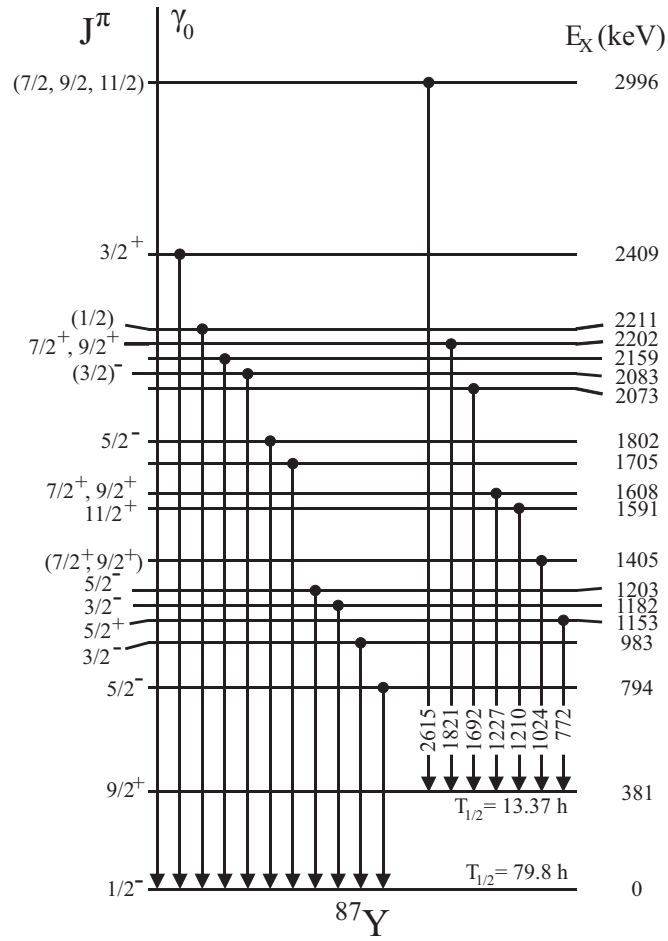

FIG. 5. Level scheme of the ^{87}Y nucleus containing all the γ transitions (vertical arrows) observed in the present work to populate its $1/2^-$ ground state and the first excited $9/2^+$ metastable level. These transitions were used to determine the cross sections σ_g for the production of ^{87}Y in its ground state and σ_m for its production in the metastable state. The excitation energies in keV indicated at the right of the levels as well as the spins and parities shown on their left were taken from [15].

with $T_{1/2} = 15.663(5)$ s at an excitation energy of 909 keV, which populates its ground state via an $M4 + E5$ γ transition. From the γ-angular distributions of the 909-keV γ transition we were able to determine the cross section σ_m for the production of ^{89}Y in this metastable state. This cross section was not reported in [10] but is given in the present work. The γ-angular distributions analyzed in the present work were obtained by measuring γ-singles spectra at eight angles θ with respect to the beam direction. From these spectra, the areas under the relevant peaks were determined and were subsequently corrected for the corresponding detector efficiency ε and the corresponding number N_b of the incoming beam particles. The latter quantity was determined by measuring the beam current and further integrating it over the measurement time by means of a current integrator. This way, the data points $I(\theta, \varepsilon, N_b)$ of the angular distribution of each γ transition were obtained and subsequently fitted by the sum of Legendre

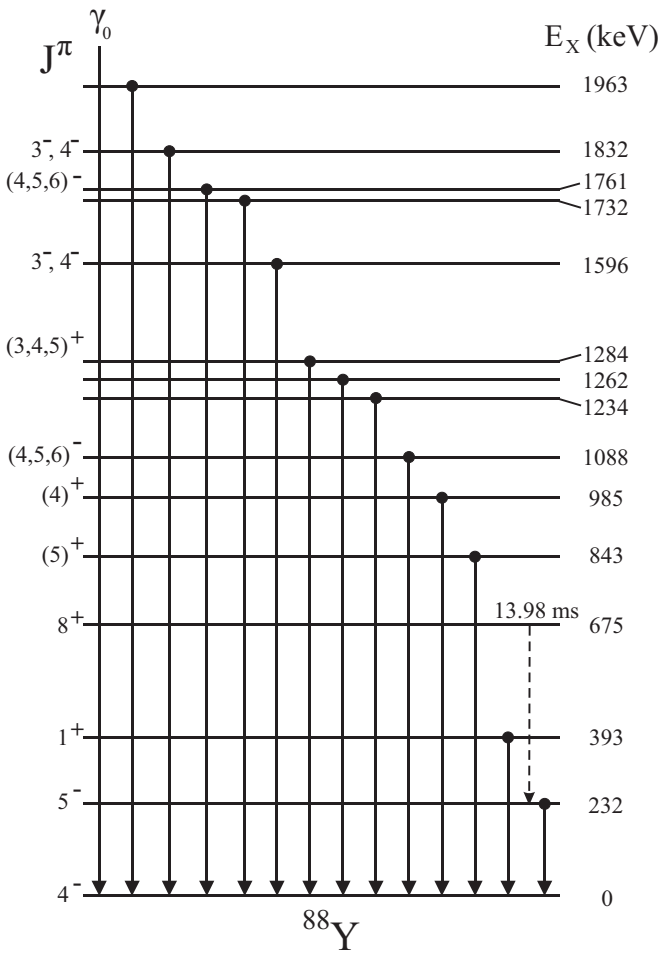

FIG. 6. Same as in Fig. 5 but for ^{88}Y. The dashed arrow indicates the γ transition deexciting the metastable state at 675 keV ($T_{1/2}$ = 13.98 ms). According to [15], the corresponding 442.6-keV γ ray is an $E3$ γ transition.

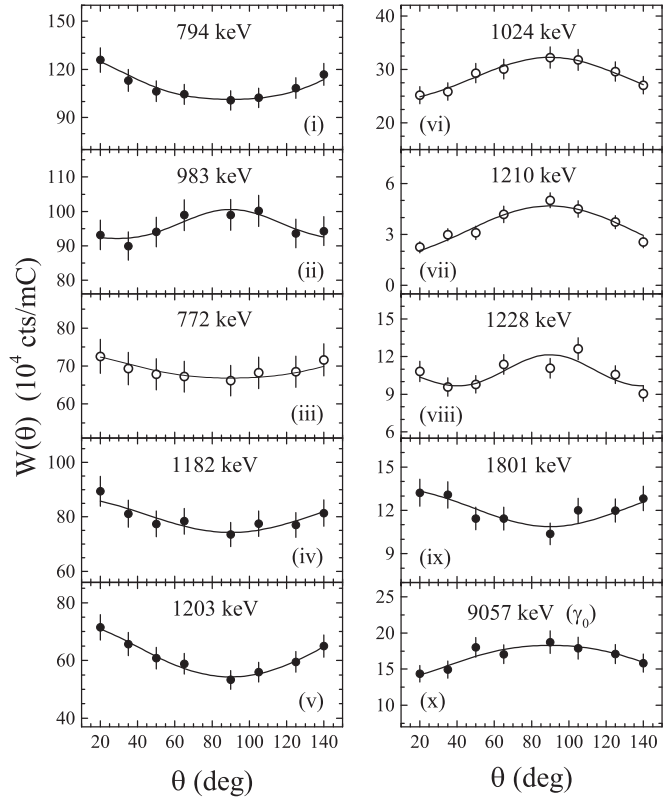

FIG. 7. Typical angular distributions of γ transitions depopulating excited levels in the ^{87}Y nucleus produced with the ^{86}Sr$(p,\gamma)^{87}$Y reaction at E_p = 3.3 MeV. The primary γ ray from the entry to the ground state is shown in panel (x).

polynomials $P_k(\theta)$ given by

$$W(\theta) = A_0\left(1 + \sum_k a_k P_k(\theta)\right). \quad (4)$$

The coefficients A_0 and a_k entering Eq. (4) are determined by fitting $W(\theta)$ to $I(\theta, \varepsilon, N_b)$. Both coefficients are energy dependent and the maximum value of index k, with $k \geqslant 2$, depends on the multipolarity of the γ transition in consideration.

The A_0 coefficients determined by this fitting procedure were used to derive Y_T using Eq. (2) for ^{87}Sr$(p,\gamma)^{88}$Y and ^{88}Sr$(p,\gamma)^{89}$Y and Eq. (3) for ^{86}Sr$(p,\gamma)^{87}$Y. Some typical γ-angular distributions measured in the present work for the ^{86}Sr$(p,\gamma)^{87}$Y and ^{87}Sr$(p,\gamma)^{88}$Y reactions are shown in Figs. 7 and 8, respectively. Typical γ-angular distributions measured previously for the ^{88}Sr$(p,\gamma)^{89}$Y are given in Ref. [10].

As shown in Fig. 8, for many γ transitions deexciting discrete levels in ^{88}Y, the angular distribution effects were not significant. In these cases, the necessary A_0 coefficients were derived from the weighted mean $\overline{W}$ of the data points $I(\theta, \epsilon, N_p)$ of the corresponding γ-angular distribution. Hence, the horizontal lines displayed in Fig. 8 for all γ transitions except those in the two top panels (i) and (vi) indicate the corresponding $\overline{W}$ used in Eq. (2) or (3). It is worth noting that, as shown in [8], when the angular distribution effects are negligible, the weighted mean $\overline{W}$ and the A_0 coefficient derived from fitting $W(\theta)$ of Eq. (4) to $I(\theta, \varepsilon, N_b)$ deviate by less than 5%.

The determination of cross sections from γ spectra measured with the 4π γ-summing method is much simpler: Instead of measuring at least five γ spectra at each beam energy and further analyzing numerous γ transitions, one needs to acquire only one spectrum and analyze only one γ peak, i.e., the sum peak. Its intensity I_Σ is used to determine the total reaction yield Y_T from

$$Y_T = \frac{I_\Sigma}{N_b \varepsilon_\Sigma}, \quad (5)$$

where N_b is the number of the beam particles and ε_Σ is the sum-peak efficiency.

In most of the cases, the area Y_T below the γ_{Σ_0} peaks (see Figs. 3 and 4) was determined by integrating the counts in the respective channels after subtracting the background. In the case of the γ_{Σ_1} peaks, it was necessary to perform a fitting with two Gaussians to simulate the first escape peak from

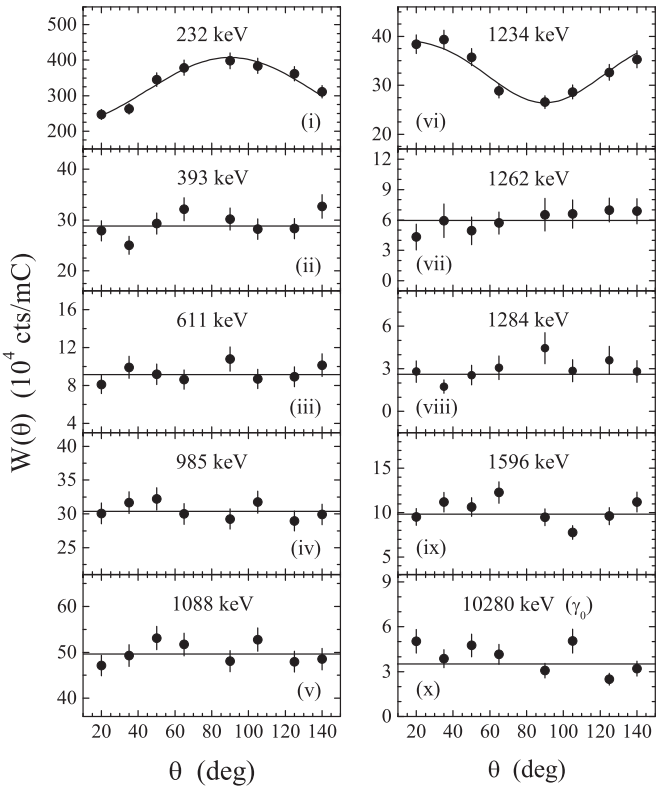

FIG. 8. Same as in Fig. 7 but for ^{88}Y produced with the ^{87}Sr$(p,\gamma)^{88}$Y reaction at $E_p = 3.6$ MeV.

the neighboring γ_{Σ_0}. The background below the sum peaks of interest was subtracted through a linear interpolation as shown in Fig. 4 for the sum peak γ_{Σ_0} of the spectrum taken at 3.2 MeV or the γ_{Σ_1} peak measured at 4.2 MeV.

The total cross section σ_T is derived by inserting Y_T in Eq. (1). In case of multiple sum peaks due to the existence of long-lived ($T_{1/2} \gtrsim 300$ ns) metastable states in the produced compound nucleus, Eq. (3) needs to be applied accordingly. A detailed presentation of the data analysis procedures followed in cross section measurements that were carried out using the 4π γ-summing technique is given in Refs. [2,9,11].

The experimental total and metastable cross sections and the corresponding astrophysical S factors obtained for the ^{86}Sr$(p,\gamma)^{87}$Y, ^{87}Sr$(p,\gamma)^{88}$Y, and ^{88}Sr$(p,\gamma)^{89}$Y reactions are summarized in Tables II, III, IV, and V. The errors given therein range between 10% and 15% and are the result of error propagation in the used equation, depending on the method applied. Hereby, the relative uncertainties in the detector efficiency ϵ_γ and the accumulated charge Q were ≈3% and ≈5%, respectively. In addition to the results listed in these tables, partial cross sections for all individual γ transitions analyzed in the present work are shown in Figs. 9, 10, and 11

Both the cross sections and astrophysical S factors given in Tables II, III, IV, and V are corrected for screening effects (Refs. [17–19]) as described in [8]. These effects result in an increase of the cross section and, hence, a correction is necessary by dividing the experimental cross sections with the corresponding electron screening factors f_s. These were calculated as described in [8] using an electron screening potential of ≈300 eV. As this value can be questioned theoretically or experimentally, f_s is explicitly given in Tables II, III, IV, and V.

The astrophysical S factors given in these tables were determined from the electron-screening-corrected cross sections

TABLE II. Screening corrected cross sections σ_T, σ_g, and σ_m, determined in the present work at various center-of-mass energies $E_{\text{c.m.}}$ (1st column) together with the corresponding astrophysical S factors S_T, S_g, and S_m and the screening correction factors f_s (2nd column), of the ^{86}Sr$(p,\gamma)^{87}$Y reaction. σ_T (3rd column) is the total cross section of the reaction, whereas σ_g (5th column) and σ_m (7th column) are the cross sections to the ground state and the 381-keV $J^\pi = 9/2^+$ isomeric state of ^{87}Y, respectively. The corresponding S factors are given in the 4th, 6th, and 8th columns. The uncertainties in $E_{\text{c.m.}}$ amount to 5 keV at the most.

$E_{\text{c.m.}}$ (MeV)	f_s	σ_T (μb)	S_T (10^3 MeV b)	σ_g (μb)	S_g (10^3 MeV b)	σ_m (μb)	S_m (10^3 MeV b)
Results obtained using the $4\pi\gamma$-summing technique							
2.464	1.057	178 ± 31	10600 ± 1850	149 ± 33	8870 ± 1960	29 ± 8	1730 ± 476
2.959	1.043	697 ± 98	6150 ± 865	549 ± 99	4850 ± 874	148 ± 23	1310 ± 203
3.454	1.034	1738 ± 268	3530 ± 545	1294 ± 283	2630 ± 575	445 ± 96	904 ± 195
Results From γ-angular distribution measurements							
2.479	1.056	183 ± 7	10190 ± 374	150 ± 6	8354 ± 334	33 ± 3	1838 ± 167
2.578	1.053	255 ± 8	9304 ± 294	207 ± 7	7553 ± 255	48 ± 4	1751 ± 146
2.677	1.050	357 ± 10	8731 ± 249	293 ± 9	7164 ± 229	64 ± 4	1568 ± 98
2.776	1.047	431 ± 11	7249 ± 193	351 ± 11	5900 ± 177	80 ± 5	1349 ± 76
2.876	1.045	542 ± 14	6364 ± 165	432 ± 13	5065 ± 151	111 ± 6	1299 ± 66
2.975	1.043	696 ± 17	5823 ± 139	548 ± 15	4584 ± 127	148 ± 7	1239 ± 57
3.074	1.040	888 ± 21	5396 ± 130	687 ± 19	4173 ± 118	201 ± 9	1222 ± 55
3.174	1.039	1080 ± 26	4823 ± 115	837 ± 24	3738 ± 106	243 ± 10	1085 ± 45
3.273	1.037	1270 ± 30	4243 ± 102	980 ± 28	3274 ± 94	290 ± 12	969 ± 40
3.372	1.035	1546 ± 37	3915 ± 93	1196 ± 34	3028 ± 86	350 ± 14	887 ± 34
3.471	1.034	1842 ± 43	3580 ± 84	1400 ± 40	2721 ± 78	442 ± 17	859 ± 33
3.570	1.032	2078 ± 48	3136 ± 72	1573 ± 44	2374 ± 66	505 ± 19	762 ± 29

TABLE III. Same as in Table II but for the ^{87}Sr$(p,\gamma)^{88}$Y reaction investigated with the 4π γ-summing technique in the present work. The σ_m given in the 7th column is the cross sections to the $J^\pi = 8^+$ isomeric state of ^{88}Y at 675 keV.

$E_{\rm c.m.}$ (MeV)	f_s	σ_T (μb)	S_T (10^3 MeV b)	σ_g (μb)	S_g (10^3 MeV b)	σ_m (μb)	S_m (10^3 MeV b)
2.566	1.053	572 ± 125	21970 ± 4783	549 ± 186	21060 ± 4775	24 ± 7	909 ± 274
2.764	1.048	982 ± 213	17275 ± 3755	940 ± 318	16531 ± 3749	42 ± 12	744 ± 206
2.962	1.043	1612 ± 350	14114 ± 3064	1540 ± 522	13487 ± 3059	72 ± 19	627 ± 167
3.160	1.039	1134 ± 242	5295 ± 1128	1061 ± 360	4953 ± 1124	73 ± 20	342 ± 95
3.358	1.035	1289 ± 278	3400 ± 734	1212 ± 415	3198 ± 732	77 ± 22	202 ± 57
3.555	1.032	1249 ± 264	1957 ± 414	1155 ± 393	1810 ± 412	94 ± 25	147 ± 39
3.753	1.030	1571 ± 336	1527 ± 327	1466 ± 501	1426 ± 326	105 ± 29	102 ± 28
3.951	1.028	1903 ± 404	1191 ± 253	1752 ± 599	1097 ± 251	151 ± 44	95 ± 28
4.149	1.026	2057 ± 431	858 ± 180	1884 ± 641	785 ± 179	173 ± 46	72 ± 19
4.940	1.020	1640 ± 351	175 ± 37	1485 ± 520	158 ± 55	158 ± 37	17 ± 5

σ using

$$S(E) = \sigma(E)\, E\, e^{2\pi\eta(E)}. \tag{6}$$

The $E_{\rm c.m.}$ values given in Tables II, III, IV, and V are the corresponding effective beam energies $E_{\rm eff}$ in the center-of-mass system. $E_{\rm eff}$ was deduced from

$$E_{\rm eff} = E_p - \frac{\Delta E}{2}, \tag{7}$$

where E_p is the incident proton beam energy and $\Delta E/2$ is its energy loss at the center of the target. The latter was derived from the stopping powers calculated with the code SRIM [12]. Typical ΔE values for $E_p = 3$ MeV, are given in Table I.

TABLE IV. Same as in Table II but for the total cross section σ_T of the ^{87}Sr$(p,\gamma)^{88}$Y reaction determined from γ-angular distributions in the present work. The corresponding S factors are given in the fourth column.

$E_{\rm c.m.}$ (MeV)	f_s	σ_T (μb)	S_T (10^3 MeV b)
1.982	1.080	39 ± 8	29113 ± 5749
2.081	1.074	68 ± 12	27990 ± 4763
2.179	1.069	107 ± 17	25583 ± 3961
2.280	1.064	182 ± 27	25856 ± 3860
2.379	1.060	244 ± 35	21447 ± 3100
2.479	1.056	394 ± 57	21952 ± 3191
2.578	1.053	523 ± 73	19104 ± 2665
2.676	1.050	725 ± 95	17851 ± 2345
2.810	1.046	993 ± 142	14767 ± 2114
2.877	1.045	1121 ± 155	13127 ± 1817
2.978	1.043	1561 ± 210	12954 ± 1740
3.016	1.042	1880 ± 255	13777 ± 1867
3.056	1.041	1419 ± 196	9138 ± 1264
3.142	1.039	1353 ± 191	6669 ± 939
3.176	1.039	1216 ± 168	5405 ± 745
3.317	1.036	1365 ± 199	4030 ± 587
3.373	1.035	1186 ± 171	2999 ± 433
3.474	1.034	1242 ± 188	2399 ± 364
3.570	1.032	1446 ± 218	2185 ± 329

IV. DISCUSSION

The comparison of experimental cross sections with the corresponding HF calculations is an important step towards understanding the discrepancies between the p-nuclei abundances observed in the solar system and those predicted by the different p-process nucleosynthesis models. This is because, regardless of any shortcomings of the astrophysics models, these discrepancies could be partly attributed to nuclear physics uncertainties entering the HF calculations. For this reason, it is essential to perform systematic comparisons between measured and calculated cross sections over the entire Gamow energy window, which is the range of energies at which charged-particle reactions contribute to the p process at a given temperature.

In this work, the (p,γ) cross sections of Sr isotopes were measured at energies in the Gamow window which

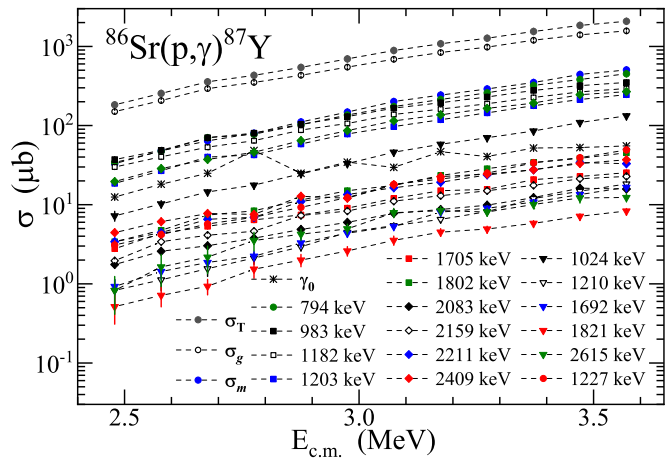

FIG. 9. Partial cross sections measured in the present work for all the γ transitions observed to populate either the ground or the metastable state of ^{87}Y through the ^{86}Sr$(p,\gamma)^{87}$Y (see also Fig. 5). The energies of the γ transitions in keV and the corresponding symbols in the plot are given in the legend. The symbols σ_T, σ_g, and σ_m refer to the total cross section and the cross sections to the ground state and to metastable levels, respectively, whereas γ_0 is for the primary γ ray from the entry to the ground state.

TABLE V. Same as in Table II but for the ^{88}Sr$(p,\gamma)^{89}$Y reaction. The σ_m given in the seventh column is the cross section to the $J^\pi = 9/2^+$ isomeric state of ^{89}Y having an excitation energy of 909 keV. The total cross sections σ_T resulting from γ-angular distribution measurements were taken from our previous publication [10] and are given here again but after having been corrected for screening effects with the corresponding factor f_s given in the second column.

$E_{\text{c.m.}}$ (MeV)	f_s	σ_T (μb)	S_T (10^3 MeV b)	σ_g (μb)	S_g (10^3 MeV b)	σ_m (μb)	S_m (10^3 MeV b)
Results obtained using the $4\pi\gamma$-summing technique							
2.478	1.053	169 ± 31	9484 ± 1740	148 ± 32	8306 ± 1796	21 ± 5	1178 ± 281
2.979	1.048	630 ± 83	5219 ± 688	515 ± 87	4267 ± 721	115 ± 17	953 ± 141
3.552	1.043	1817 ± 263	2876 ± 416	1428 ± 276	2260 ± 437	389 ± 73	616 ± 116
3.952	1.039	3026 ± 387	1894 ± 242	2285 ± 406	1430 ± 254	741 ± 127	464 ± 79
4.561	1.035	4407 ± 617	863 ± 121	3367 ± 648	659 ± 127	1040 ± 193	204 ± 38
Results from γ-angular distribution measurements							
1.379	1.141	0.55 ± 0.10	57658 ± 10483	0.50 ± 0.10	52417 ± 10483	0.05 ± 0.04	5242 ± 4193
1.479	1.126	0.8 ± 0.1	29958 ± 3745	0.73 ± 0.10	27337 ± 3745	0.07 ± 0.05	2621 ± 1872
1.580	1.114	2.0 ± 0.3	29354 ± 4403	1.82 ± 0.30	26712 ± 4403	0.18 ± 0.06	2642 ± 881
1.680	1.103	2.9 ± 0.4	18358 ± 2532	2.7 ± 0.4	17092 ± 2532	0.20 ± 0.06	1266 ± 380
1.780	1.094	7.6 ± 0.8	22334 ± 2351	7 ± 0.8	20571 ± 2351	0.60 ± 0.13	1763 ± 382
1.880	1.087	14.4 ± 1.6	20935 ± 2326	12.9 ± 1.6	18755 ± 2326	1.5 ± 0.2	2181 ± 291
1.982	1.080	15.5 ± 1.7	11637 ± 1276	13.9 ± 1.7	10436 ± 1276	1.6 ± 0.3	1201 ± 225
2.080	1.074	45 ± 5	18777 ± 2086	41 ± 5	17108 ± 2086	4 ± 1	1669 ± 417
2.180	1.069	56 ± 6	13389 ± 1434	50 ± 6	11954 ± 1434	6 ± 1	1434 ± 239
2.280	1.064	128 ± 12	18214 ± 1708	114 ± 12	16222 ± 1708	14 ± 1	1992 ± 142
2.380	1.060	149 ± 14	13056 ± 1227	134 ± 14	11742 ± 1227	15 ± 1	1314 ± 88
2.480	1.056	159 ± 15	8845 ± 834	137 ± 15	7621 ± 834	22 ± 2	1224 ± 111
2.561	1.054	196 ± 18	7700 ± 707	172 ± 18	6757 ± 707	24 ± 2	943 ± 79
2.581	1.053	188 ± 17	6796 ± 614	162 ± 17	5856 ± 614	26 ± 2	940 ± 72
2.680	1.050	348 ± 31	8449 ± 753	300 ± 32	7284 ± 777	48 ± 3	1165 ± 73
2.780	1.047	394 ± 36	6545 ± 598	341 ± 37	5665 ± 615	53 ± 4	880 ± 66
2.880	1.045	504 ± 49	5848 ± 569	409 ± 49	4745 ± 569	95 ± 7	1102 ± 81
2.957	1.043	588 ± 54	5242 ± 481	486 ± 54	4333 ± 481	102 ± 7	909 ± 62
2.980	1.042	640 ± 68	5285 ± 562	520 ± 69	4294 ± 570	120 ± 8	991 ± 66
3.081	1.040	980 ± 87	5841 ± 519	795 ± 88	4738 ± 524	185 ± 11	1103 ± 66
3.180	1.038	992 ± 90	4363 ± 396	782 ± 91	3440 ± 400	210 ± 13	924 ± 57
3.281	1.037	1235 ± 113	4043 ± 370	972 ± 114	3182 ± 373	263 ± 17	861 ± 56
3.354	1.035	1275 ± 120	3402 ± 320	1009 ± 121	2692 ± 323	266 ± 17	710 ± 45
3.380	1.035	1391 ± 128	3456 ± 318	1091 ± 129	2710 ± 320	300 ± 19	745 ± 47
3.478	1.034	2013 ± 181	3852 ± 346	1549 ± 183	2964 ± 350	464 ± 28	888 ± 54
3.552	1.032	1714 ± 163	2713 ± 258	1347 ± 164	2132 ± 260	367 ± 24	581 ± 38
3.750	1.030	2117 ± 192	2076 ± 188	1630 ± 195	1599 ± 191	487 ± 31	478 ± 30
3.948	1.028	2851 ± 225	1799 ± 142	2136 ± 229	1348 ± 145	715 ± 44	451 ± 28
4.146	1.026	3539 ± 291	1486 ± 122	2588 ± 297	1087 ± 125	951 ± 59	399 ± 25
4.344	1.024	4551 ± 373	1309 ± 107	3292 ± 381	947 ± 110	1259 ± 77	362 ± 22
4.541	1.022	4118 ± 326	834 ± 66	3142 ± 332	636 ± 67	976 ± 62	198 ± 13
4.739	1.021	4222 ± 329	615 ± 48	3270 ± 334	477 ± 49	952 ± 60	139 ± 9
4.937	1.020	2638 ± 218	282 ± 23	1962 ± 222	210 ± 24	676 ± 43	72 ± 5

extends from ≈2.6 to 4.2 MeV. In the case of ^{87}Sr$(p,\gamma)^{88}$Y and ^{88}Sr$(p,\gamma)^{89}$Y reactions, cross sections were measured over the entire Gamow window, whereas in the case of ^{86}Sr$(p,\gamma)^{87}$Y they were measured up to 3.6 MeV.

The experimental cross sections were used to test the OMP, NLD, and γSF models that enter the HF calculations. Of special interest to nuclear astrophysics are the corresponding (semi)microscopic models that are based on a more fundamental microscopic treatment of the nucleon-nucleon interaction and nuclear structure properties such as pairing and nuclear deformation. Although these models also use adjustable parameters to fit the available data, they use fewer parameters, which combined with the microscopic nature of the models allows for a more reliable extrapolation to mass regions which are not yet accessible in the laboratory and for which no measurements exist.

The reaction networks involved in the *p*-process abundance calculations include almost 2000 nuclei between Ge and Bi, so, in addition to being semimicroscopic, the models used in HF calculations should also be "global" in nature and reproduce the average properties of all these ≈2000 nuclei many of which lie beyond the valley of stability.

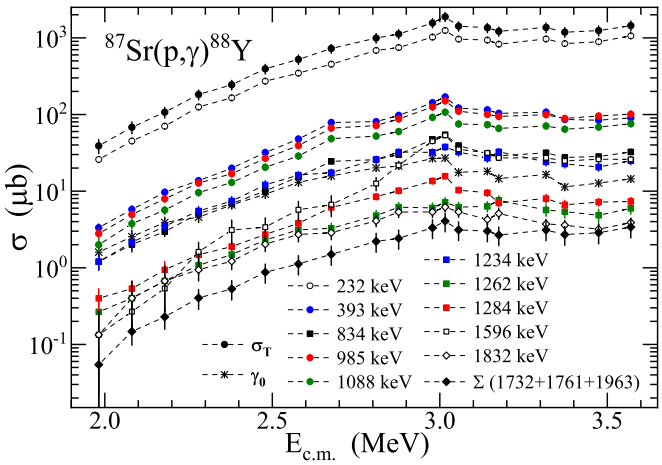

FIG. 10. Same as in Fig. 9 but for the ^{87}Sr$(p,\gamma)^{88}$Y reaction. Σ(1732+1761+1963) corresponds to the sum of the cross sections of the three γ rays with energies given in the parentheses (see also Fig. 6).

Our plan is to investigate the impact of global semimicrosopic models for nucleon-nucleus OMPs, NLDs, and γSFs on HF calculations in comparison to global phenomenological models in order to make recommendations for the currently available models in the literature. This is a challenging task mainly because of the lack or scarcity of experimental data that would allow us to fix the parameters of the OMPs, NLDs, and γSF models independently without having to use the reaction cross-section data themselves. The difficulty with using reaction cross-section data is that they are sensitive to all three nuclear ingredients of the HF theory (OMPs, NLDs, and γSFs) over most of the relevant energy region.

As has been demonstrated in previous works [8,46], it is possible to distinguish between proton-nucleus optical model potentials (pOMPs), if the comparison between measured and calculated cross sections is conducted at properly selected proton energies. At the lowest energies of the Gamow window relevant to proton-induced reactions, where the (p, n) channel is closed and the (p, p') and (p, α) channels are much weaker than the (p, γ) channel, the HF cross section depends almost entirely on the pOMP. In such a case, it is possible to test the pOMPs and improve them by comparing them with the (p, γ) data data, provided the latter are reliable. If the above conditions are not fulfilled, i.e., if the (p, γ) is of comparable strength to the (p, p') or (p, α) or if the (p, n) channel is open, then the other HF ingredients, i.e., NLDs and γSFs, also influence the HF cross section and the independent improvement of the pOMP is not possible. In this work, we shall optimize the parameters of a semimicroscopic proton OMP to our measured data and use this local pOMP in our assessment of global semi-microscopic models of the three HF ingredients.

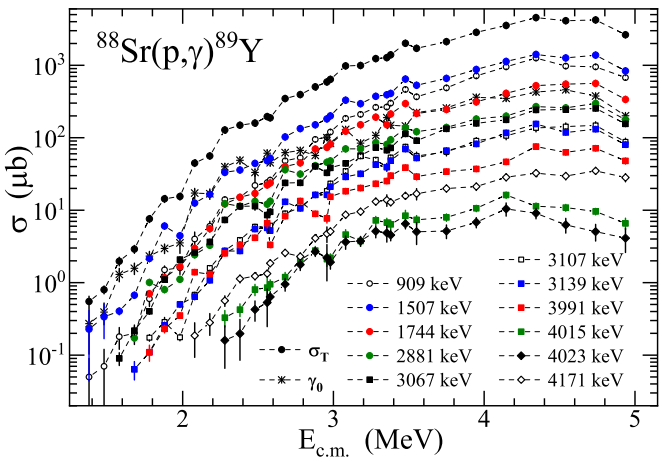

FIG. 11. Same as in Fig. 9 but for the ^{88}Sr$(p,\gamma)^{89}$Y reaction.

For our calculations we use the latest version 1.95 of the nuclear reaction code TALYS [5] and all the nuclear models available therein. All the experimental cross sections used have been corrected for screening effects, as described in [8]. This applies also to the total cross-section data reported previously by Galanopoulos *et al.* [10] for ^{88}Sr$(p,\gamma)^{89}$Y (open circles), and the data measured by the activation method by Gyürky *et al.* [21] (open squares).

In Fig. 12, we compare TALYS calculations with our experimental total cross sections determined by measuring γ-angular distributions (open circles) or with the 4π γ-summing technique (black solid circles). The calculated cross sections (dashed curves) shown in all four panels are obtained with the default options of the TALYS code for incident charged particles, i.e., the nucleon-nucleus OMP of Koning and Delaroche [20], the α-particle–nucleus OMP of Avrigeanu *et al.* [22], the constant temperature Fermi gas model for NLDs [4], and γSFs based on the generalized Lorentzian model of Kopecky and Uhl [23]. For the needs of our discussion, these models are labeled henceforth as KD, AV/I, CTFG, and KU, respectively. Their combination, abbreviated as KD–AV/I–CTFG–KU, is a pure phenomenological one and is referred to as "TALYS default."

As can be seen in Fig. 12, the TALYS default (KD–AV/I–CTFG–KU) calculations are in reasonable agreement with our present data and those reported in Ref. [10]. The shaded areas shown in the figure are the areas corresponding to the HF cross sections obtained by using all the combinations of the KD OMP with all the αOMP, NLD, and γSF models available in TALYS 1.95. These areas give an estimate of how certain (narrow area) or uncertain (broad area) our knowledge of the cross sections is based on the models that are available in TALYS 1.95. A complete list of these models with the corresponding notation is given in Table VI.

The arrows shown in panels (a) and (b) of Fig. 12 indicate the opening of the corresponding (p, n) channel. For the case of ^{86}Sr$(p,\gamma)^{88}$Y and ^{84}Sr$(p,\gamma)^{85}$Y this occurs at 6.02 and 7.54 MeV, respectively. The dashed-dotted lines shown in the figure correspond to the (p, p') cross sections calculated using the TALYS default model combination. The (p, α) cross sections are negligible in the studied energy ranges, therefore they will not be included in the discussions.

The differences observed between the cross sections measured with the activation technique [21] (open squares) and those determined with the other two methods (open circles and solid black circles), in the case of the ^{87}Sr$(p,\gamma)^{88}$Y reaction

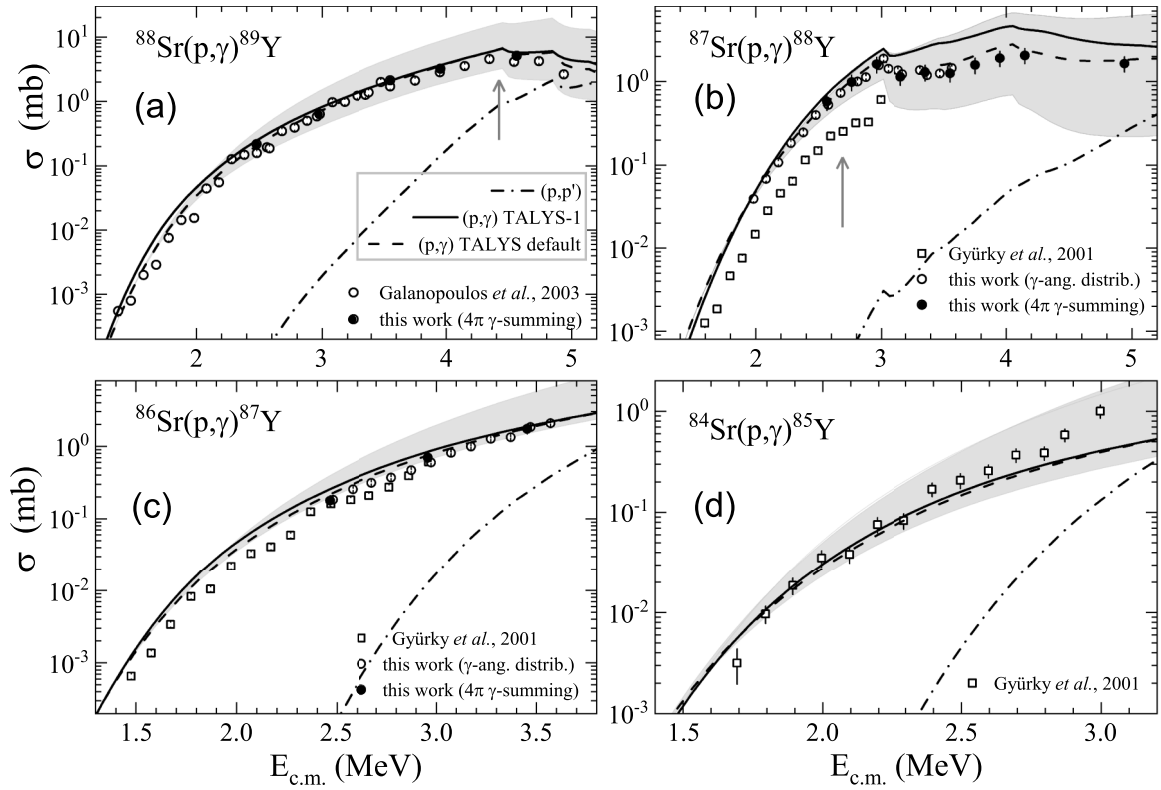

FIG. 12. Comparison of experimental cross sections determined for ^{88}Sr$(p,\gamma)^{89}$Y, ^{87}Sr$(p,\gamma)^{88}$Y, ^{86}Sr$(p,\gamma)^{87}$Y, and ^{84}Sr$(p,\gamma)^{85}$Y with HF calculations performed with the TALYS 1.95 code [5]. The dashed curves indicate cross sections calculated with TALYS 1.95 using the default model combination KD–AV/I–CTFG–KU (TALYS default). The dashed-dotted curves depict the (p,p') cross sections calculated using TALYS default. The solid curves, labeled "TALYS-1," were calculated using the combination JLM/Bc–AV/I–CTFG–KU. The shaded areas depict the area covered by the cross sections obtained using all possible combinations of the KD OMP with all the αOMP, NLD, and γSF models given in Table VI (see also text for details).

(see Fig. 12), are resolved if the former cross sections are multiplied by a factor ≈2.5.

Deviations between these different measurements are also visible for ^{86}Sr$(p,\gamma)^{87}$Y. In this case, the data from the activation technique [21] are lower than the present data by an overall factor of ≈1.4. A possible explanation for these deviations could be the lower yields measured in the activity measurements [21] due to the significantly shorter irradiation periods (between 6 and 24 hours) compared to the half-lives of ^{87}Y and ^{88}Y, which are 79.8 h and 106.626 d, respectively.

A. Testing the proton–nucleus OMP

According to Fig. 12, all the combinations of the KD OMP with the various NLD and γSFs available in TALYS give identical results in the very low energy region, implying that in this region the HF cross sections are sensitive to the proton OMP in the incident channel only. The onset of effects arising from the γSF in the proton capture channel and the NLDs in all open channels is visible at $E_{c.m} \approx 2$, 2.2, and 1.8 MeV, in panels (a), (b), and (c), respectively. Therefore, the experimental data measured at energies below these onset energies could be used to test different pOMP models.

In panel (d), this onset becomes visible already at $E_{c.m} \approx$ 1.6 MeV. Therefore, the ^{84}Sr$(p,\gamma)^{85}$Y reaction cannot be used to distinguish between different pOMP models since there are not enough data points measured below 1.6 MeV. It is worth mentioning that these energy onsets (limits) do not change significantly when using a different pOMP, i.e., when using the TALYS-1 model combination in which the OMP of Koning and Delaroche [20] is replaced by the Lane-consistent semi-microscopic model of Bauge, Delaroche and Girod [35,36].

The solid curves plotted in Fig. 12 were calculated by replacing the phenomenological OMP of Koning and Delaroche [20] by the semimicroscopic OMP of Bauge, Delaroche, and Girod (JLM/B) [35,36] in the TALYS default combination. We used the improved JLM/B OMP of Vagena *et al.* [46] for this comparison, as it has been shown to improve the proton-induced cross sections at low energies relevant to our studies compared to the original parametrization of [35,36]. The improved proton OMP (pOMP) of [46] is based on a re-adjustment of the parameters $\lambda_{v,w}$ of the real and imaginary isoscalar parts of the proton OMP to reproduce the bulk of available (p,γ) and (p,n) cross-section data. Systematics of the variation of these $\lambda_{v,w}$ parameters with respect to the mass number A were established over a relatively broad mass region $47 \leqslant A \leqslant 162$. According to [46], the adjustment factor f_v has a mass number dependence which can be described by a second degree polynomial in the mass region $A \leqslant 100$

TABLE VI. Nuclear input parameters (first column) and corresponding phenomenological or semimicroscopic models used in our TALYS calculations. The nucleon-nucleus and α-particle–nucleus optical model potentials (OMPs) are indicated with nOMP and αOMP, respectively. The corresponding model notation used for discussion in Sec. V is given in parentheses.

Parameter	Phenomenological models	Semimicroscopic models
nOMP	(1) (KD): Global model of Koning and Delaroche [20]	(2) (JLM/Bc): Improved semimicroscopic OMP of Bauge, Delaroche, and Girod at low energies [46]
αOMP	(1) (WKD): TALYS-specific α-particle–nucleus OMP (folding procedure of Watanabe [26,27] applied to KD [20]) (2) (McFS): α-particle–nucleus OMP of McFadden and Satchler [28] (3) (AV/I): α-particle–nucleus OMP of Avrigeanu *et al.* [22] (4) (Nlt): α-particle–nucleus OMP of Nolte *et al.* [29] (5) (AV/II): α-particle–nucleus OMP of Avrigeanu *et al.* [30]	(6) (αOMP-I): Demetriou *et al.* (Table 1 of Ref. [37]) (7) (αOMP-II): Demetriou *et al.* (Table 2 of Ref. [37]) (8) (αOMP-III): Demetriou *et al.* (dispersive model in Ref. [37])
NLD	(1) (CTFG): Constant temperature Fermi gas [4] (2) (BSFG): Back-shifted Fermi gas [31,32] (3) (GSM): Generalized superfluid model [33,34]	(4) (HFBCS): Hartree-Fock-BCS [38] (5) (HFB): Hartree-Fock-Bogolyubov [39] (6) (HFB/T): Temperature-dependent Hartree-Fock-Bogolyubov [40]
γSF	(1) (KU): Generalized Lorentzian of Kopecky and Uhl [23] (2) (BA): Generalized Lorentzian of Brink and Axel [24,25]	(3) (HFBCS/QRPA): Hartree-Fock-BCS–quasiparticle random-phase approximation [41] (4) (HFB/QRPA): Hartree-Fock-Bogolyubov–quasiparticle random-phase approximation [42] (5) (HG): Hybrid model of Goriely [43] (6) (HFB/T): Temperature-dependent Hartree-Fock-Bogolyubov [42] (7) (RMF/T): Temperature-dependent RMF [44] (8) (D1M/HFB/QRPA): Gogny D1M Hartree-Fock-Bogolyubov–quasiparticle random-phase approximation [45]

and by a logarithmic increase for $A > 100$. In addition, although f_w appears to have a small effect on the calculations, a global increase by 50% improves the results for certain nuclei without affecting the rest of the cases. In the case of the Sr isotopes, the values of the adjustment factors are $f_v = 0.8$ and $f_w = 1.5$. The resulting combination of pOMP JLM/Bc with the other default ingredients, abbreviated as JLM/Bc–AV/I–CTFG–KU, is henceforth referred to as "TALYS-1."

A comparison of TALYS default and TALYS-1 combinations in the aforementioned low energy regions in panels (a), (b), and (c) in Fig. 12 shows that TALYS default reproduces the experimental data well and in any case slightly better than TALYS-1, which appears to overestimate the data. Since both combinations differ only in the pOMP, we conclude that the improved semi-microscopic pOMP JLM/Bc [46] leads to a slight overestimation of the data, at least at energies below $\approx$2.5 MeV. This is not entirely unexpected, since the improved pOMP [46] is based on global systematics with respect to mass A covering a broad mass range, and the deduced values of $\lambda_{v,w}$ have uncertainties associated with the limited number and quality of the experimental available data.

In the following, we optimize the JLM/B pOMP to reproduce our experimental data for the Sr isotopes at the low energies below the onset of effects from the other nuclear ingredients becoming visible. The parameters that will be deduced will be"local," i.e., optimal for the Sr isotopes, as opposed to the "global" parameters of [46]. For this task, it is important to have reliable experimental data; therefore, we only consider the cross sections for the ^{88}Sr$(p,\gamma)^{89}$Y reaction in panel (a) and exclude the data for reactions ^{87}Sr$(p,\gamma)^{88}$Y and ^{86}Sr$(p,\gamma)^{88}$Y in panels (b) and (c) due to the aforementioned deviations between the activation data [21] and the cross sections determined in the present work.

The general functional form of the Lane-consistent JLM/B OMP [35,36] is given by

$$U = \lambda_v[V_0 \pm \lambda_{v1}\alpha V_1] + i\lambda_w[W_0 \pm \lambda_{w1}\alpha W_1] + U_{\rm so}, \quad (8)$$

where V_0, W_0 and V_1, W_1 are the real and imaginary isoscalar and isovector components of the central potential seen by a neutron (proton) and $U_{\rm so}$ is the component due to spin-orbit interaction. $\lambda_{v,w}$ and $\lambda_{v1,w1}$ are the normalization factors for the real, imaginary, real isovector and imaginary isovector

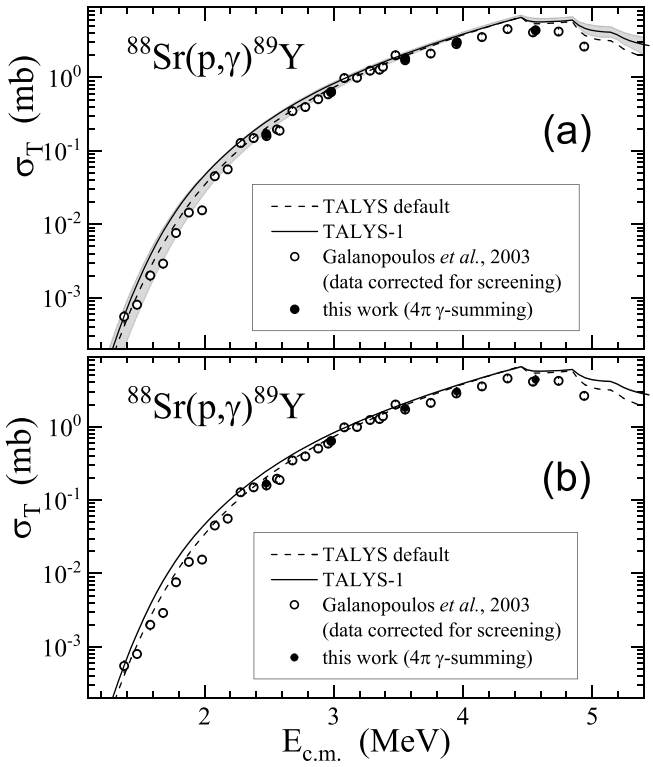

FIG. 13. Comparison of the experimental total cross sections determined for ^{88}Sr$(p,\gamma)^{89}$Y in the present work (solid circles) and in [10] (open circles) after correction for screening effects with the corresponding calculations using the model combinations TALYS default (dashed curve) and TALYS-1 (solid curve). The shaded area in panel (a) depicts the range of cross section values obtained with TALYS-1 by varying f_v between 0.9 and 1.1 and keeping $f_w = 1$. In panel (b), $f_v = 1$, whereas f_w was varied between 0.9 and 1.1. The resulting shaded area is hardly visible in panel (b). See also text.

components introduced to adjust the OMP to experimental data. These normalization factors are energy dependent.

We adjusted only the isoscalar factors $\lambda_{v,w}$ to improve the description of the cross-section data since the isovector $\lambda_{v1,w1}$ factors have been found to have a negligible effect on the cross sections. We then used the TALYS-1 model combination and performed two tests: first we varied λ_v within a range of 10% by introducing a multiplicative factor f_v that ranged between 0.9 and 1.1 and kept λ_w unchanged at the TALYS 1.95 default value; then as a second test we simply reversed the case and varied λ_w by 10% using a multiplicative factor f_w from 0.9 to 1.1 and kept λ_v unchanged. The results of these two tests are shown in panels (a) and (b) of Fig. 13, respectively.

The shaded area in panel (a) of Fig. 13 depicts the range of cross section values resulting from varying λ_v in the first test, whereas in panel (b) it shows the corresponding range obtained in the second test by varying λ_w within 10%. According to panel (a), a variation of 10% in λ_v values results in a significant increase or decrease in the cross sections at energies below ≈2.5 MeV or higher than ≈5 MeV. We found that the resulting cross sections at $E_{\mathrm{c.m.}} = 1$, 2, and 3 MeV can be smaller by up to 65%, 45%, and 20%, respectively, if $f_v \approx 0.9$.

TABLE VII. Semimicroscopic model combinations of NLDs and γSFs used to calculate reaction cross sections in the present work. In all combinations the local optimized OMP of of Bauge *et al.* [35,36] and the α-particle–nucleus OMP-III of Demetriou *et al.* [37] were used. The abbreviations given in columns 2 and 3 are explained in Table VI.

Model combination abbreviation	NLD model	γSF model
TALYS-2	HFBCS [38]	HFBCS/QRPA [41]
TALYS-3	HFB [39]	HFB/QRPA [42]
TALYS-4	HFB/T [40]	HFB/T [42]
TALYS-5	HFB/T [40]	RMF/T [44]
TALYS-6	HFB [39]	D1M/HFB/QRPA [45]
TALYS-7	HFB [39]	HG [43]
TALYS-8	HFBCS [38]	HG [43]

As can be seen in panel (a) of Fig. 13, the slope of the TALYS default curve becomes slightly steeper at low energies and the agreement with the experimental data can be improved significantly by properly adjusting λ_v. On the other hand, the impact of f_w is not as important, as the cross sections do not differ significantly when varying f_w between 0.9 and 1.1; the corresponding shaded area in panel (b) is hardly visible. In this case the resulting cross sections deviate less than 3% at all energies above 0.5 MeV.

Based on Fig. 13, the *p*OMP of Bauge *et al.* [35,36] can be optimized at low energies by identifying the optimum value for the normalization factor λ_v of the isoscalar real part of the potential. Additional fine tuning could be achieved by varying the normalization factor λ_w of the isoscalar imaginary part but it would not affect the cross sections significantly. Our search for an optimum value of λ_v yielded a value of $f_v = 1.1$, i.e., a 10% increase of λ_v. This is a 37% increase with respect to the global adjusted value $f_v = 0.8$ of [46]. The λ_w parameter remains unchanged, hence $f_w = 1$ compared to $f_w = 1.5$ of [46]; however, as was also mentioned in the latter publication, the increase of f_w only affects very few nuclides and not the Sr isotopes.

After having improved the semimicroscopic JLM/B OMP as described above, we proceeded to investigate whether a combination of purely (semi)microscopic models of OMPs, NLDs, and γSFs can successfully reproduce the experimental data across the whole range of measured energies. Ideally, one hopes to find one combination of OMPs, NLDs, and γSFs capable of reproducing the (p,γ) cross sections for all Sr isotopes. The semimicroscopic model options offered by TALYS 1.95 are listed in the third column of Table VI. If we omit αOMP-I and II and only consider αOMP-III, which is a dispersive αOMP, we end up with 18 model combinations.

In our analysis, however, we only used the combinations listed in Table VII, which we consider to be to some extent self-consistent in terms of the microscopic models used to calculate the nuclear ground-state properties. Such is the combination of the global HFBCS NLD and HFBCS/QRPA γSF models in Table VI. Both are based on the same Hartree-Fock-BCS model using the same effective Skyrme interaction for the description of the ground-state properties and are in this

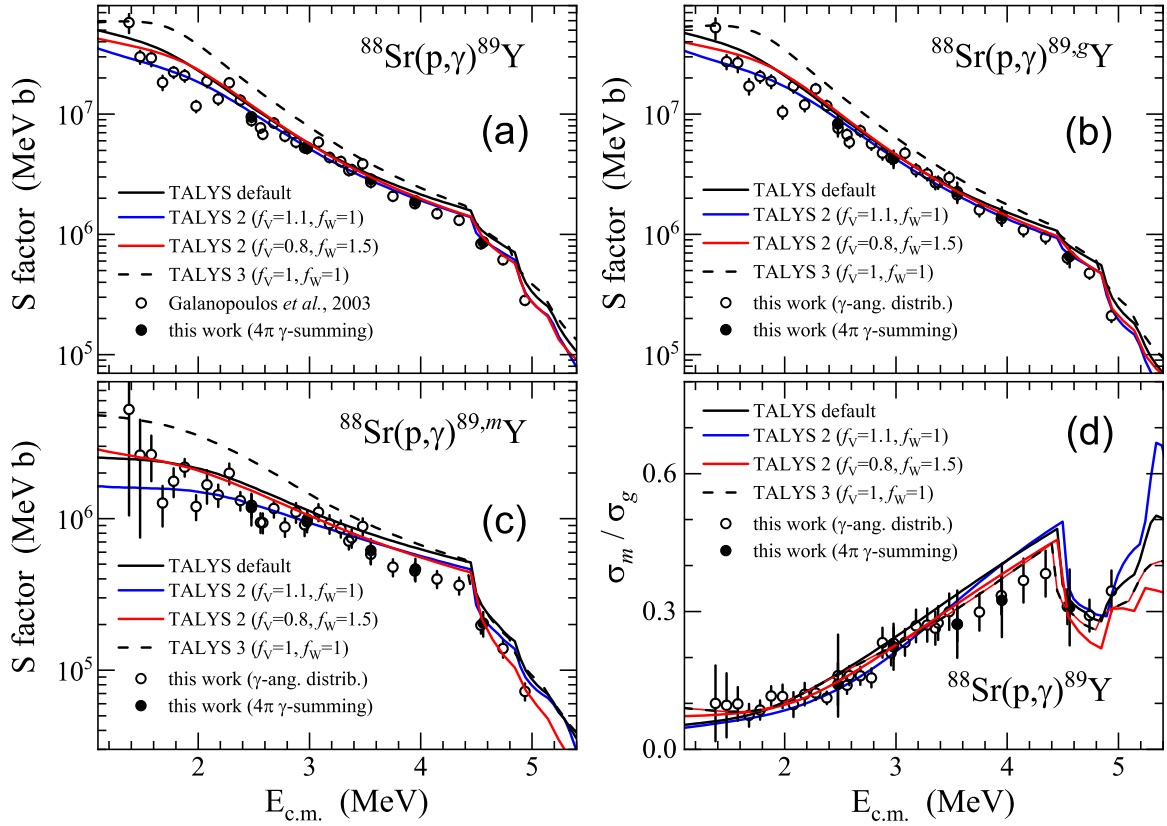

FIG. 14. Comparison of the experimental cross section data determined in the present work for ^{88}Sr$(p,\gamma)^{89}$Y with the corresponding calculations (blue curve) performed with the TALYS-2 model combination and $f_v = 1.1$ and $f_w = 1$. The black curve indicates the TALYS default combination, whereas the red one corresponds to the TALYS-2 combination but with $f_v = 0.8$ and $f_w = 1.5$, as recommended in [46]. In addition, the dashed black curve shows the results using the TALYS-3 model combination that was found to be the best one for the reproduction of our previous cross section results in the Se [8] and Mo [9] isotopes. Panel (a) depicts the astrophysical S_T factor obtained from the total cross section, whereas panels (b) and (c) show the astrophysical S_g and S_m factors given in Table V. In panel (d), the experimental metastable-to-ground cross section ratio is compared with the corresponding TALYS calculations (see also text).

sense consistent. Similarly, the combination of HFB NLDs and HFB/QRPA γSFs is also self-consistent since they are both based on the same HFB model for the ground-state properties.

The αOMP-III has also been updated to include proton and neutron density distributions based on the same HFB model in the double-folding calculations. Therefore, combination TALYS-3 in Table VII is self-consistent among three out of four nuclear ingredients. Obviously, it is not possible to attain 100% consistency among all the semimicroscopic models used for OMPs, NLDs, and γSFs, therefore the list in Table VII contains partially self-consistent models.

The results of our attempt to optimize the semimicroscopic OMP of Bauge, Delaroche, and Girod [35,36] and identify a purely semimicroscopic model combination from those listed in Table VII that reproduces successfully the experimental data for ^{88}Sr$(p,\gamma)^{89}$Y are shown in Fig. 14. Hereby, we plot astrophysical S factors instead of cross sections, for a more transparent comparison between our experimental data and these calculations, because cross sections cover five orders of magnitude in scale in contrast to the S factors which extend over only three orders of magnitude. In panels (a), (b), and (c) of Fig. 14, the depicted S factors are, respectively, the S_T, S_g, and S_m factors, as given in Table V. In addition, the experimental isomeric-to-ground cross-section ratio is compared with the corresponding calculations.

The best model combination found in our analysis for ^{88}Sr$(p,\gamma)^{89}$Y is plotted in Fig. 14 with a blue curve that corresponds to TALYS-2 with $f_v = 1.1$, $f_w = 1$. For comparison, the purely phenomenological TALYS default cross sections are also plotted as a black solid curve. In every panel of Fig. 14 we include two more TALYS calculations, plotted as dashed-black and red curves. The former corresponds to the "standard" ($f_v = 1$, $f_w = 1$) TALYS-3 combination, which was found to be the best semi-microscopic model combination in our last two investigations in the Se [8] and Mo [9] isotopes and is given also here for an easier systematic comparison of (p,γ) reactions below mass $A = 100$.

The red curves depicted in all panels of Fig. 14 correspond to the best model combination resulting when $f_v = 0.8$ and $f_w = 1.5$ are used according to the global systematics of [46]. In this case too, the best TALYS model combination for the reaction ^{88}Sr$(p,\gamma)^{89}$Y is TALYS-2, i.e., the same as for the local optimization of the pOMP using $f_v = 1.1$ and $f_w = 1$.

Similar analyses were performed for the ^{87}Sr$(p,\gamma)^{88}$Y and ^{86}Sr$(p,\gamma)^{87}$Y reactions and the results are shown in Figs. 15

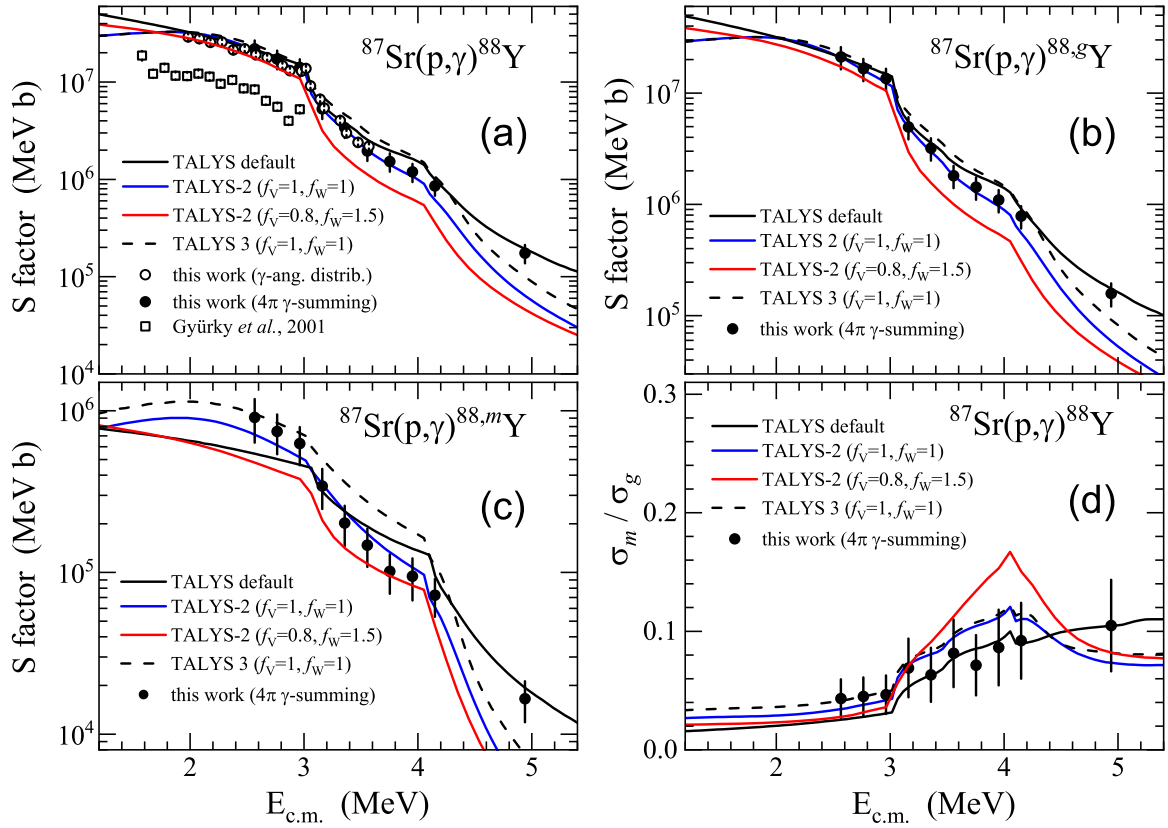

FIG. 15. Same as in Fig. 11 but for the ^{87}Sr$(p,\gamma)^{88}$Y.

and 16, respectively. In the former case, TALYS-3 is the best model combination, with $f_v = 1$ and $f_w = 1$, as well as with $f_v = 0.8$ and $f_w = 1.5$. For the latter reaction, we found similarly that TALYS-5 is the best model combination.

The data for the reaction ^{84}Sr$(p,\gamma)^{85}$Y that were published in [21] were also analyzed using the same approach after having been corrected for screening effects. In this case, however, there is no single combination of input parameters that can describe reasonably well all the three types of measured cross sections, namely, the total, ground state (g.s.), and metastable cross sections. It is not clear whether this is due to an issue with the measurements, or due to shortcomings in the spin distribution of the NLD models. In Fig. 17, we compare the ^{84}Sr$(p,\gamma)^{85}$Y data with the TALYS default and the two TALYS-4 combinations which gave the best results among all the other combinations in Table VII. The comparison shows conflicting trends in the calculated cross sections to the g.s. and metastable states that lead to large deviations between calculated and experimental ratios of metastable to g.s. cross sections. These findings require further investigation that is beyond the scope of this paper.

The best combinations of NLD and γSF models found above can be validated by comparing their results for other derived quantities, such as total radiative widths Γ_γ, s-wave resonance spacings D_0, and cumulative number of low-lying levels, which are relevant at low excitation energies below or around the neutron separation energy. Unfortunately, for the compound nuclei populated by the (p,γ) reactions on ^{88,87,86,84}Sr isotopes, i.e., for ^{89,88,87,85}Y, there are limited experimental data available.

Due to the lack of measured average radiative widths, in Fig. 18 we compare the calculated average radiative widths with systematics [47]. As can be seen in the figure, the calculated Γ_γ values agree with the systematics for the compound nuclei ^{88,89}Y populated in the (p,γ) reactions on ^{87,88}Sr while for ^{85,87}Y, populated in the respective reactions on ^{84,86}Sr, they disagree by almost a factor of 2. Since the average radiative width is an integral over the γSF and NLD, it depends both on the γSF and the NLD model used, therefore we cannot discern if the disagreement observed in Fig. 18 for the lighter isotopes of Y is due to the γSF or the NLD or both models.

On the other hand, experimental γSF data have been extracted for ^{89}Y by means of charged-particle reactions, NRF, and (p,γ) reactions as shown in Fig. 19. The γSF obtained from the HFBCS/QRPA model of [41] (in combination TALYS-2) agrees with the experimentally extracted data within the experimental uncertainties. These results, combined with those shown in Fig. 19, indicate that the HFBCS/QRPA model of [41] used in TALYS-2, can describe low-energy γ emission from the compound nucleus ^{89}Y fairly well. Although the extracted experimental γSF data also depend on NLD and other model assumptions implemented in the different measurement techniques, within the range of uncertainties they provide constrains for the theoretical models as shown in Fig. 19. Additional effort is needed however, to extend

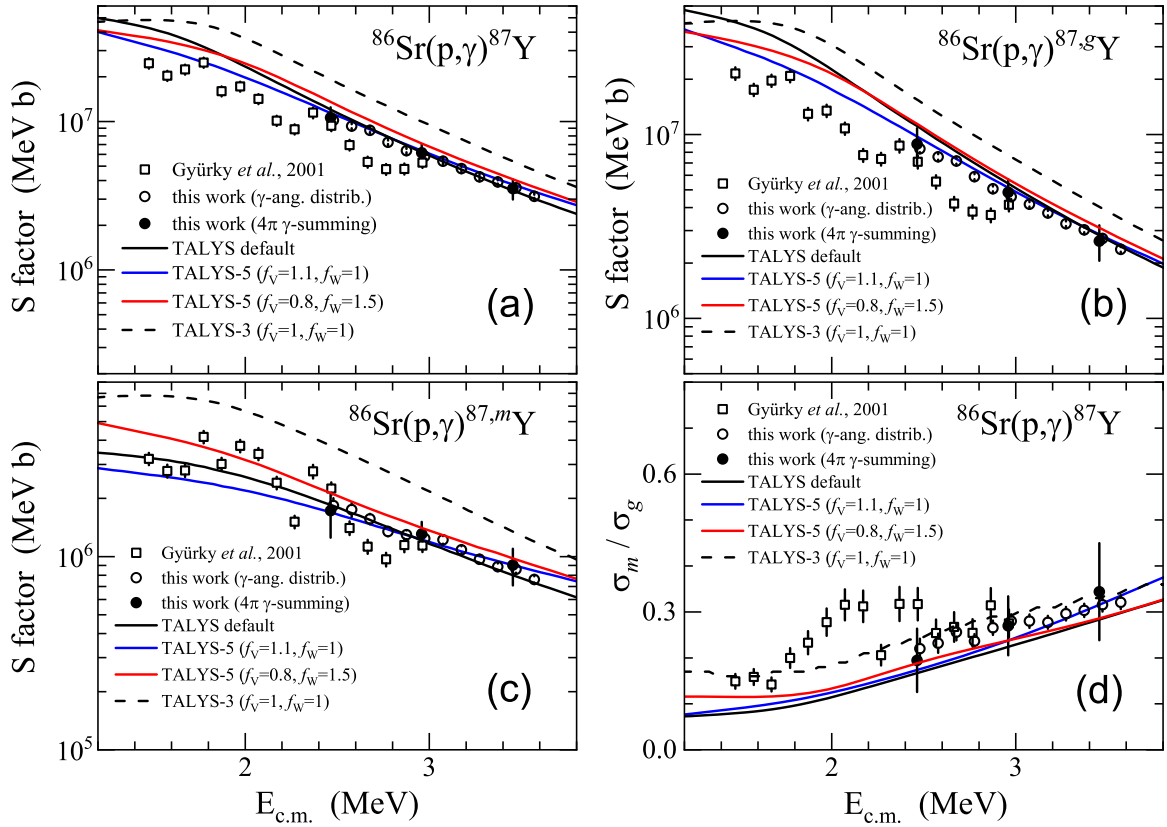

FIG. 16. Same as in Fig. 11 but for the ^{86}Sr$(p,\gamma)^{87}$Y for which TALYS-5 was found to reproduce the data the best (see also text).

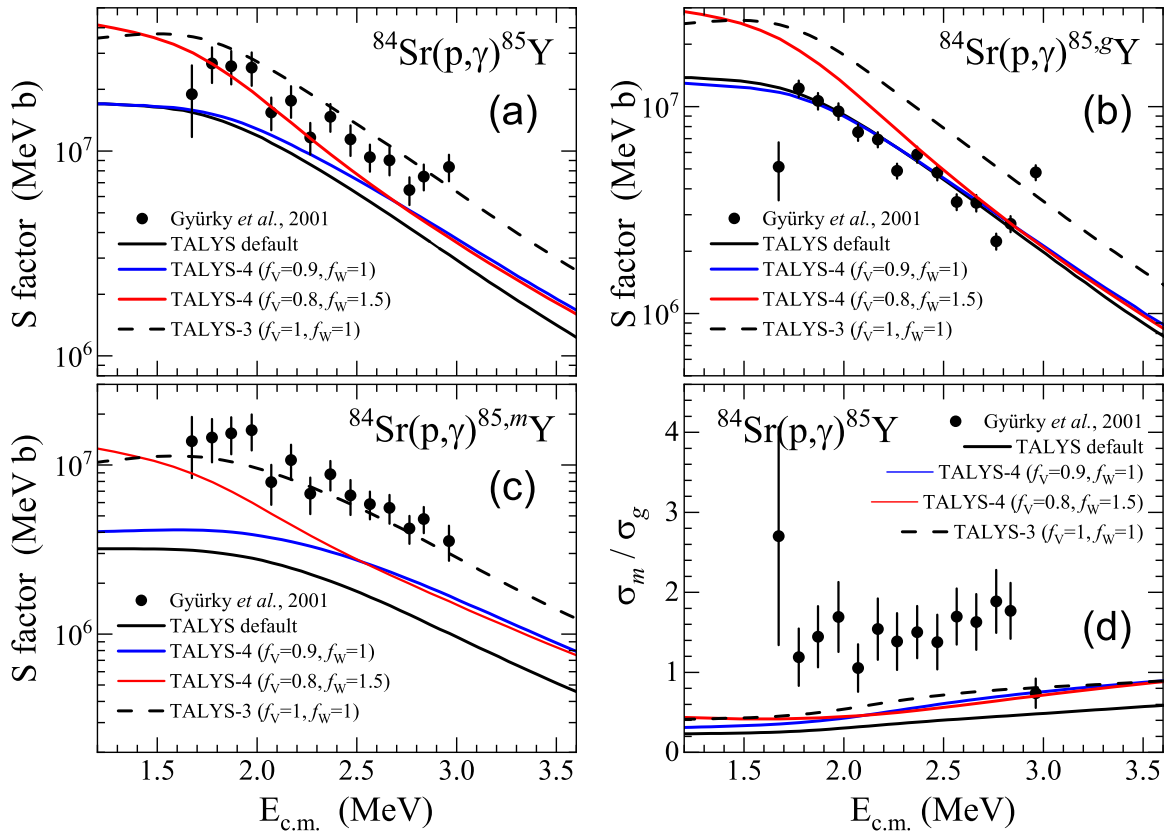

FIG. 17. Same as in Fig. 11 but for the ^{84}Sr$(p,\gamma)^{87}$Y for which TALYS-4 was found to better reproduce the experimental data (see also text).

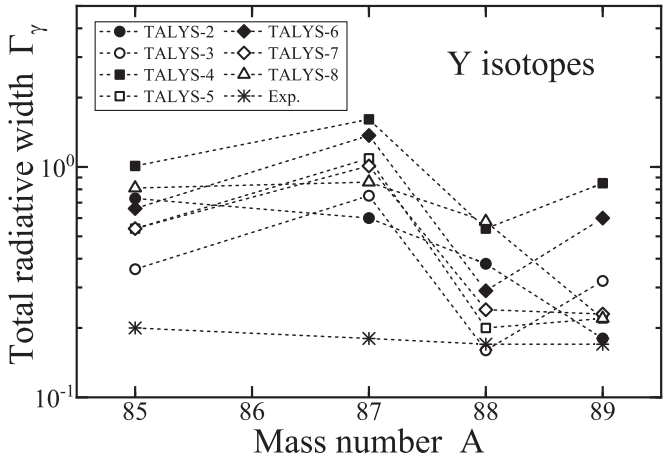

FIG. 18. Total radiative widths Γ_γ of ^{85,87,88,89}Y isotopes calculated with the best combinations found in the present work are compared with systematics from Ref. [47].

such measurements to a wider range of nuclei, both stable and unstable. The experimental γSF data used in the comparison were taken from the online IAEA database [48].

The validation of the NLD models for the relevant compound and residual nuclei ^{85,87,88,89}Y is possible at the low excitation energies involving discrete low-lying states. In Fig. 20, the cumulative number $N_{\rm cum}$ of observed low-lying states for ^{85,87,88,89}Y are compared with the results of the NLD models used in the best combinations found in this work, i.e., TALYS-4, -5, -3, and -2, respectively. As can be seen in the figures, the NLD models can reproduce the low-energy part of the available phase space in the Y compound nuclei reasonably well. The NLDs based on semimicroscopic models obviously do not provide a smooth increase reminiscent of the constant-temperature model; however, they reproduce the overall trend and in some of the cases, such as ^{89}Y, are in excellent agreement with the cumulative number of observed low-lying states. Due to lack of experimental D_0 data for the

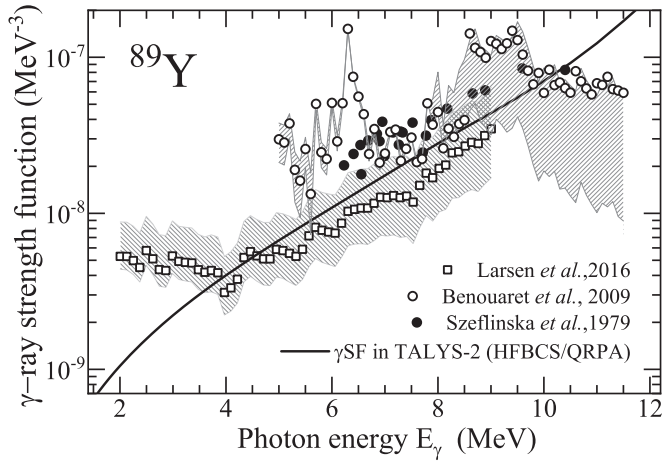

FIG. 19. Comparison of the dipole strength function f_1 obtained from the HFBCS/QRPA model with the available experimental data extracted using the Oslo method [49], NRF [50], and (p,γ) measurements [51]. The experimental γSFs were taken from the IAEA PSF database [48].

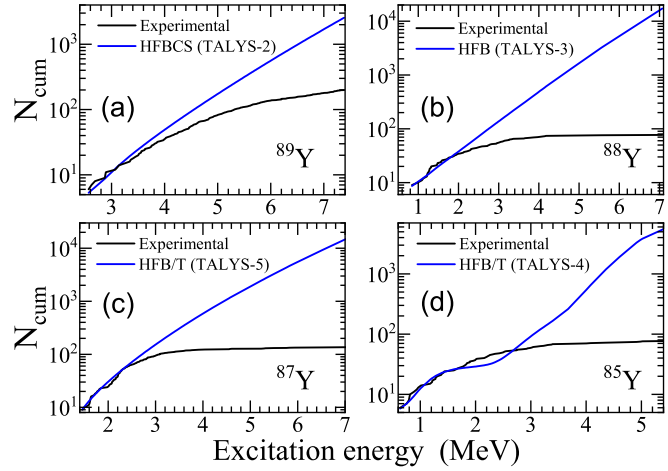

FIG. 20. Comparison of the cumulative number ($N_{\rm cum}$) of observed low-lying levels with NLD models used in the best combinations found in this work for compound and residual nuclei ^{85,87,88,89}Y.

Y isotopes, we are unable to constrain or make any meaningful comparison of the NLDs at higher excitation energies around S_n, which are more relevant to the compound nucleus reactions at the energies studied in the present work.

B. Reaction rates

Reaction rates are the key nuclear quantities used in p-process abundance calculations. For this purpose, reaction rate libraries such as BRUSLIB [52] and REACLIB [53] have been developed and widely used in the last decades. Both libraries provide stellar rates for almost any proton capture reaction.

BRUSLIB rates are calculated with the TALYS code using the phenomenological nucleon-nucleus OMP of Koning and Delaroche [20], the global semimicroscopic models of Demetriou, Grama, and Goriely [37] for the α-particle–nucleus OMP, the Hartree-Fock-Bogolyubov (HFB) model for NLDs [39], and the $E1$-strength function from the HFB/QRPA calculation of Ref. [42].

REACLIB reaction rates are calculated with the NON-SMOKER$^{\rm WEB}$ HF code (version 5.0w) [54]. This code uses the microscopic OMP of Jeukenne *et al.* [55,56], the phenomenological model of McFadden and Satchler for the α-particle–nucleus OMP [28], and the phenomenological γSF and NLD models from Refs. [57,58], respectively.

In Fig. 21, we plot various ratios of the total stellar reaction rates from the BRUSLIB and REACLIB databases with the corresponding rates obtained in this work with the best semimicroscopic model combinations as well as with those derived with the semimicroscopic model combinations using the global values $f_v = 0.8$, $f_w = 1.5$ recommended by Vagena *et al.* [46].

The solid blue curve in panel (a) of Fig. 21 depicts the ratio of the BRUSLIB [52] total stellar reaction rates of ^{88}Sr$(p,\gamma)^{89}$Y over the corresponding rates determined in the present work with TALYS2 and the "local" values $f_v = 1.1$, $f_w = 1$. The solid red curve is the similar ratio of the REACLIB [53] rates. Accordingly, the dotted blue and dotted red curves

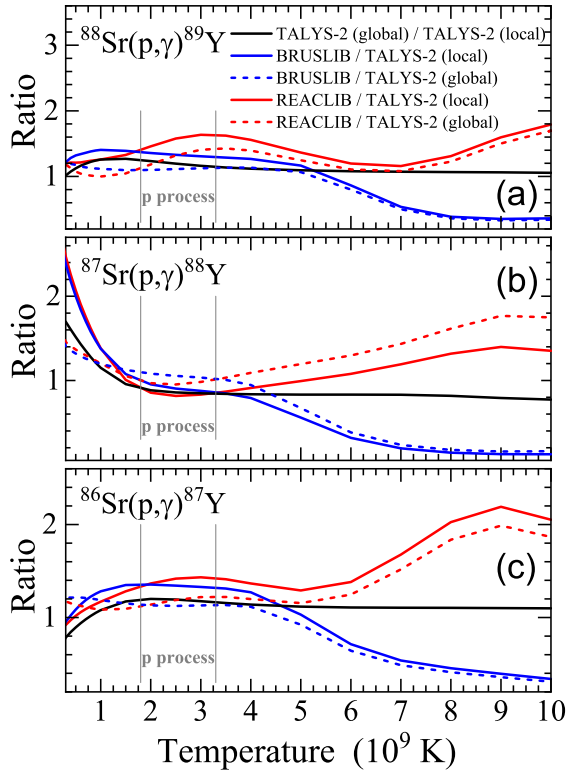

FIG. 21. Ratios of the stellar reaction rates of the BRUSLIB [52] and REACLIB [53] databases over the stellar rates obtained for the three (p, γ) reactions investigated in the present work using the semimicroscopic model combinations found to reproduce the best the (p, γ) reaction cross sections determined in the present work (see text for details).

depict the ratio of the BRUSLIB and REACLIB total stellar reaction rates over the corresponding ones calculated with TALYS2 and the "global" values $f_v = 0.8$, $f_w = 1.5$ recommended by Vagena *et al.* [46]. In addition, we also plot the ratio of the TALYS-2 (global) to TALYS-2 (local) results with a solid black curve. The legend in panel (a) applies to the other two panels (b) and (c) for the ^{87}Sr$(p, \gamma)^{88}$Y and ^{86}Sr$(p, \gamma)^{87}$Y reactions investigated in the present work. The two grey vertical lines shown in every panel indicate the temperature region where *p* process occurs.

According to panel (a) of Fig. 21, in the temperature region relevant to *p* process, the TALYS2 "global" rates deviate from the TALYS2 "local" ones up to 25%. Moreover, the corresponding REACLIB rates deviate the most (60%), whereas in the case of BRUSLIB the relevant ratio does not exceed 1.35. Both the REACLIB and BRUSLIB rates show smaller deviations when compared with the TALYS2 "global" ones.

In the case of ^{87}Sr$(p, \gamma)^{88}$Y shown in panel (b), the REACLIB rates do not deviate more than 20% from the TALYS2 "local" ones and much less (5%) from the TALYS2 "global" rates. The BRUSLIB rates deviate less than 10% in both cases, whereas the TALYS2 "global" ones deviate from those of TALYS2 "local" by 15% at the most. Finally, as shown by the ratios plotted in panel (c) for ^{86}Sr$(p, \gamma)^{87}$Y, the corresponding deviations lie between those observed in the two previous cases.

Based on Fig. 21, it can be concluded that the total stellar reaction rates given in the REACLIB database are deviating the most from those derived by using the semimicroscopic model combinations that were found to reproduce the best the (p, γ) reaction cross sections determined in the present work.

V. CONCLUSIONS

In the present work the total cross sections of proton capture reactions on ^{86}Sr, ^{87}Sr, and ^{88}Sr isotopes were determined at energies relevant to *p*-process nucleosynthesis from γ-angular distribution measurements and angle-integrated γ spectra taken with the 4π γ-summing technique [2]. The cross sections to the corresponding isomeric and ground states were also determined and the relevant isomeric cross-section ratios were derived.

Our cross-section data and the resulting astrophysical *S* factors were compared with Hauser-Feshbach (HF) calculations obtained with the latest version 1.95 of the nuclear reaction code TALYS [4,5] using combinations of global semimicroscopic and phenomenological models of optical potentials (OMPs), nuclear level densities (NLDs), and γ-ray strength functions (γSFs).

Overall, a good agreement was found between our data and the TALYS cross sections obtained with the phenomenological nucleon-nucleus OMP of Koning and Delaroche [20], the αOMP of Avrigeanu *et al.* [22], the constant temperature Fermi gas (CTFG) model for NLDs [4], and the γSFs based on the generalized Lorentzian of Kopecky and Uhl (KU) [23].

The Lane-consistent semimicroscopic OMP of Bauge, Delaroche, and Girod [35,36] was optimized to reproduce our experimental data for ^{88}Sr$(p, \gamma)^{89}$Y at the lowest energies measured, where its predictions were deviating by almost 50% from data. This was achieved by varying the normalization factors λ_v and λ_w for the real and imaginary isoscalar components of the central OMP.

This new local semimicroscopic *p*OMP was then combined with global, semimicroscopic, and consistent NLD and γSF models to give equally good descriptions of the proton capture cross sections for the ^{86}Sr, ^{87}Sr, and ^{88}Sr isotopes as the global phenomenological models. In addition, we used the recently improved global semi-microscopic OMP of Bauge, Delaroche, and Girod [35,36] by [46], which also reproduces the low-energy cross sections for the (p, γ) reactions on ^{86,87,88}Sr isotopes. An optimum combination of semimicroscopic NLD and γSF along with this improved *p*OMP was found to describe the experimental cross sections fairly well. The semimicroscopic models of NLDs and γSFs in these optimal combinations were further validated by comparisons with other available independent data on low-lying observed levels and total radiative widths. However, it was not possible to identify one unique combination of semi-microscopic input models for all three Sr isotopes.

The stellar reaction rates obtained using the semimicroscopic model combinations that were found to

reproduce our experimental data the best were compared with the corresponding rates from the BRUSLIB [52] and REACLIB [53] libraries. It was found that, in the *p*-process relevant temperature region, the REACLIB stellar rates overall deviate up to 60% in the case of ^{88}Sr$(p,\gamma)^{89}$Y and around 40% for ^{86}Sr$(p,\gamma)^{87}$Y, whereas in the case of ^{87}Sr$(p,\gamma)^{88}$Y, they differ by not more than 15%. The corresponding deviations of the BRUSLIB stellar rates ware found to be 35%, 15%, and 10%, respectively.

Our results underscore the importance of performing systematic studies of proton-capture reactions for as wide a range of relevant nuclei as possible to reduce the uncertainties of global nuclear models. In this regard, new (p,γ) cross-section measurements at the lowest possible energies below the opening of the neutron channel are of key importance to improve global proton-nucleus optical model potentials. In addition, independent experimental data on NLDs and γSFs are also crucial to determining the HF ingredients at energies above the neutron threshold.

ACKNOWLEDGMENTS

We acknowledge support of this work by the project "CALIBRA/EYIE" (MIS 5002799), which is implemented under the Action "Reinforcement of the Research and Innovation Infrastructures," funded by the Operational Programme "Competitiveness, Entrepreneurship and Innovation" (NSRF 2014-2020) and cofinanced by Greece and the European Union (European Regional Development Fund).

[1] M. Arnould and S. Goriely, The *p*-process of stellar nucleosynthesis: Astrophysics and nuclear physics status, Phys. Rep. **384**, 1 (2003).

[2] Sotirios V. Harissopulos, Cross-section measurements of capture reactions relevant to *p*-process nucleosynthesis, Eur. Phys. J. Plus **133**, 332 (2018).

[3] W. Hauser and H. Feshbach, The inelastic scattering of neutrons, Phys. Rev. **87**, 366 (1952).

[4] A. J. Koning, S. Hilaire, and M. C. Duijvestijn, TALYS-1.0, in *Proceedings of the International Conference on Nuclear Data for Science and Technology*, Nice, France, 2007, edited by O. Bersillon, F. Gunsing, E. Bauge, R. Jacqmin, and S. Leray (EDP Sciences, Les Ulis, France, 2008), p. 211, available online at http://dx.doi.org/10.1051/ndata:07767.

[5] Nuclear reaction code TALYS-1.95, available online at http://www.talys.eu/home.

[6] Nuclear reaction model code EMPIRE, available online at https://www-nds.iaea.org/empire/index.html.

[7] T. Rauscher, nuclear reaction model code SMARAGD, http://nucastro.org/smaragd.html.

[8] V. Foteinou, S. Harissopulos, M. Axiotis, A. Lagoyannis, G. Provatas, A. Spyrou, G. Perdikakis, Ch. Zarkadas, and P. Demetriou, Cross section measurements of proton capture reactions on Se isotopes relevant to the astrophysical *p* process, Phys. Rev. C **97**, 035806 (2018).

[9] V. Foteinou, M. Axiotis, S. Harissopulos, P. Dimitriou, G. Provatas, A. Lagoyannis, H.-W. Becker, D. Rogalla, A. Zilges, A. Schreckling and A. Endres, Cross section measurements of proton capture reactions on Mo isotopes relevant to the astrophysical *p* process, Eur. Phys. J. A. **55**, 67 (2019).

[10] S. Galanopoulos, P. Demetriou, M. Kokkoris, S. Harissopulos, R. Kunz, M. Fey, J. W. Hammer, G. Gyürky, Z. Fülop, E. Somorjai, and S. Goriely, ^{88}Sr$(p,\gamma)^{89}$Y reaction at astrophysically relevant energies, Phys. Rev. C **67**, 015801 (2003).

[11] A. Spyrou H.-W. Becker, A. Lagoyannis, S. Harissopulos, and C. Rolfs, Cross-section measurements of capture reactions relevant to the *p* process using a $4\pi\gamma$-summing method, Phys. Rev. C **76**, 015802 (2007).

[12] J. F. Ziegler, The Stopping and Range of Ions in Matter: Code SRIM, available online at http://www.srim.org/.

[13] A. Markowicz and R. V. Grieken, *Handbook on X-Ray Spectrometry* (Marcel Dekker, New York, 1993).

[14] K. Debertin and R. Helmer, Gamma and X-ray Spectrometry with Semiconductor Detectors (North-Holland, Amsterdam 1988).

[15] IAEA Live Chart of Nuclides, Nuclear Structure and Decay Data based on the Evaluated Nuclear Structure Data File (ENSDF), https://www-nds.iaea.org/livechart/.

[16] S. Harissopulos, A. Spyrou, A. Lagoyannis, M. Axiotis, P. Demetriou, J. W. Hammer, R. Kunz, and H.-W. Becker, Cross section measurements of proton capture reactions relevant to the *p* process: The case of ^{89}Y$(p,\gamma)^{90}$Zr and ^{121,123}Sb$(p,\gamma)^{122,124}$Te, Phys. Rev. C **87**, 025806 (2013).

[17] C. E. Rolfs and W. S. Rodney, *Cauldrons in the Cosmos* (The University of Chicago Press, Chicago, 1988)

[18] C. E. Rolfs, Enhanced electron screening in metals: A plasma for the poor man, Nucl. Phys. News **16**, 9 (2006); private communication.

[19] K. U. Kettner, H. W. Becker, F. Strieder, and C. Rolfs, High-Z electron screening: The cases ^{50}V$(p,n)^{50}$Cr and ^{176}Lu$(p,n)^{176}$Hf, J. Phys. G: Nucl. Part. Phys. **32**, 489 (2006).

[20] A. J. Koning and J. P. Delaroche, Local and global nucleon optical models from 1 keV to 200 MeV, Nucl. Phys. A **713**, 231 (2003).

[21] Gy. Gyürky, E. Somorjai, Zs. Fülöp, S. Harissopulos, P. Demetriou and T. Rauscher, Proton capture cross section of Sr isotopes and their importance for nucleosynthesis of proton-rich nuclides, Phys. Rev. C **64**, 065803 (2001).

[22] V. Avrigeanu, M. Avrigeanu, and C. Mănăilescu, Further explorations of the α-particle optical model potential at low energies for the mass range $A \approx 45$–209, Phys. Rev. C **90**, 044612 (2014).

[23] J. Kopecky and M. Uhl, Test of gamma-ray strength functions in nuclear reaction model calculations, Phys. Rev. C **41**, 1941 (1990).

[24] D. M. Brink, Individual particle and collective aspects of the nuclear photoeffect, Nucl. Phys. **4**, 215 (1957).

[25] P. Axel, Electric dipole ground-state transition width strength function and 7-Mev photon interactions, Phys. Rev. **126**, 671 (1962).

[26] S. Watanabe, High energy scattering of deuterons by complex nuclei, Nucl. Phys. **8**, 484 (1958).

[27] D. G. Madland, Recent results in the development of a global medium-energy nucleon-nucleus Optical-Model Potential, in

Proceedings, Specialists' Meeting on Preequilibrium Nuclear Reactions, Semmering, Austria, 1988, edited by Brigitte Strohmaier (OECD, Paris, 1988), p. 103.

[28] L. McFadden and G. R. Satchler, Optical-model analysis of the scattering of 24.7 MeV alpha particles, Nucl. Phys. **84**, 177 (1966).

[29] M. Nolte, H. Machner, and J. Bojowald, Global optical potential for α particles with energies above 80 MeV, Phys. Rev. C **36**, 1312 (1987).

[30] V. Avrigeanu, P. E. Hodgson, and M. Avrigeanu, Global optical potentials for emitted alpha particles, Phys. Rev. C **49**, 2136 (1994).

[31] W. Dilg, W. Schantl, H. Vonach, and M. Uhl, Level density parameters for the back-shifted fermi gas model in the mass range $40 < A < 250$, Nucl. Phys. A **217**, 269 (1973).

[32] M. K. Grossjean and H. Feldmeier, Level density of a Fermi gas with pairing interactions, Nucl. Phys. A **444**, 113 (1985).

[33] A. V. Ignatyuk, K. K. Istekov, and G. N. Smirenkin, Role of the collective effects in a systematics of nuclear level densities, Yad. Fiz. **29**, 875 (1979) [Sov. J. Nucl. Phys. **29**, 450 (1979)].

[34] A. V. Ignatyuk, J. L. Weil, S. Raman, and S. Kahane, Density of discrete levels in ^{116}Sn, Phys. Rev. C **47**, 1504 (1993).

[35] E. Bauge, J. P. Delaroche, and M. Girod, Lane-consistent, semimicroscopic nucleon-nucleus optical model, Phys. Rev. C **63**, 024607 (2001).

[36] E. Bauge, J. P. Delaroche, and M. Girod, Semimicroscopic nucleon-nucleus spherical optical model for nuclei with $A \geqslant 40$ at energies up to 200 MeV, Phys. Rev. C **58**, 1118 (1998).

[37] P. Demetriou, C. Grama, and S. Goriely, Improved global α-optical model potentials at low energies, Nucl. Phys. A **707**, 253 (2002).

[38] P. Demetriou and S. Goriely, Microscopic nuclear level densities for practical applications, Nucl. Phys. A **695**, 95 (2001).

[39] S. Goriely, S. Hilaire, and A. J. Koning, Improved microscopic nuclear level densities within the Hartree-Fock-Bogoliubov plus combinatorial method, Phys. Rev. C **78**, 064307 (2008).

[40] S. Hilaire, M. Girod, S Goriely, and A. J. Koning, Temperature-dependent combinatorial level densities with the D1M Gogny force, Phys. Rev. C **86**, 064317 (2012).

[41] E. Khan, S. Goriely, D. Allard, E. Parizot, T. Suomijarvi, A. J. Koning, S. Hilaire, and M. C. Duijvestijn, Photodisintegration of ultra-high-energy cosmic rays revisited, Astropart. Phys. **23**, 191 (2005).

[42] S. Goriely, E. Khan, M. Samyn, Microscopic HFB + QRPA predictions of dipole strength for astrophysics applications, Nucl. Phys. A **739**, 331 (2004).

[43] S. Goriely, Radiative neutron captures by neutron-rich nuclei and the *r*-process nucleosynthesis, Phys. Lett. B **436**, 10 (1998).

[44] I. Daoutidis and S. Goriely, Large-scale continuum random-phase approximation predictions of dipole strength for astrophysical applications, Phys. Rev. C **86**, 034328 (2012).

[45] M. Martini, S. Péru, S. Hilaire, S. Goriely, and F. Lechaftois, Large-scale deformed quasiparticle random-phase approximation calculations of the γ-ray strength function using the Gogny force, Phys. Rev. C **94**, 014304 (2016).

[46] E. Vagena, M. Axiotis and P. Dimitriou, Systematics of the semimicroscopic proton-nucleus optical potential at low energies relevant for nuclear astrophysics, Phys. Rev. C **103**, 045806 (2021).

[47] R. Capote, M. Herman, P. Oblozinsky, P. G. Young, S. Goriely, T. Belgya, A. V. Ignatyuk, A. J. Koning, S. Hilaire, V. Plujko, M. Avrigeanu, O. Bersillon, M. B. Chadwick, T. Fukahori, S. Kailas, J. Kopecky, V. M. Maslov, G. Reffo, M. Sin, E. Soukhovitskii *et al.* RIPL - Reference input parameter library for calculation of nuclear reactions and nuclear data evaluations, Nucl. Data Sheets **110**, 3107 (2009).

[48] S. Goriely, P. Dimitriou, M. Wiedeking, T. Belgya, R. Firestone, J. Kopecky, M. Krtička, V. Plujko, R. Schwengner, S. Siem, H. Utsunomiya, S. Hilaire, S. Peru, Y. S. Cho, D. M. Filipescu, N. Iwamoto, T. Kawano, V. Varlamov, and R. Xu, Reference database for photon strength functions, Eur. Phys. J. A **55**, 172 (2019).

[49] A. C. Larsen, M. Guttormsen, R. Schwengner, D. L. Bleuel, S. Goriely, S. Harissopulos, F. L. Bello Garrote, Y. Byun, T. K. Eriksen, F. Giacoppo, A. Görgen, T. W. Hagen, M. Klintefjord, T. Renstrøm, S. J. Rose, E. Sahin, S. Siem, T. G. Tornyi, G. M. Tveten, A. V. Voinov, and M. Wiedeking, Experimentally constrained $(p,\gamma)^{89}$Y and $(n,\gamma)^{89}$Y reaction rates relevant to *p*-process nucleosynthesis, Phys. Rev. C **93**, 045810 (2016).

[50] N. Benouaret, R. Schwengner, G. Rusev, F. Dönau, R. Beyer, M. Erhard, E. Grosse, A. R. Junghans, K. Kosev, C. Nair, K. D. Schilling, A. Wagner, and N. Bendjaballah, Dipole strength in ^{89}Y up to the neutron-separation energy, Phys. Rev. C **79**, 014303 (2009).

[51] G. Szeflinska, Z. Szeflinski, Z. Wilhelmi, Gamma-ray strength functions for $A = 70$–90 nuclei, Nucl. Phys. A **323**, 253 (1979).

[52] Y. Xu, S. Goriely, A. Jorissen, G. L. Chen, and M. Arnould, Databases and tools for nuclear astrophysics applications: BRUSsels Nuclear LIBrary (BRUSLIB), Nuclear Astrophysics Compilation of REactions II (NACRE II) and Nuclear NETwork GENerator (NETGEN), Astron. Astrophys. **549**, A106 (2013).

[53] R. H. Cyburt, A. M. Amthor, R. Ferguson, Z. Meisel, K. Smith, S. Warren, A. Heger, R. D. Hoffman, T. Rauscher, A. Sakharuk, H. Schatz, F. K. Thielemann, and M. Wiescher, The Jina reaclib database: Its recent updates and impact on type-IX-ray bursts, Astrophys. J. Suppl. Ser. **189**, 240 (2010).

[54] T. Rauscher, Online code NON-SMOKER$^{\text{WEB}}$, 2008, https://nucastro.org/websmoker.html.

[55] J.-P. Jeukenne, A. Lejeune, and C. Mahaux, Microscopic calculation of the symmetry and Coulomb components of the complex optical-model potential, Phys. Rev. C **15**, 10 (1977).

[56] A. Lejeune, Low-energy optical model potential in finite nuclei from Reid's hard core interaction, Phys. Rev. C **21**, 1107 (1980).

[57] J. J. Cowan, F.-K. Thielemann, J. W. Truran, The R-process and nucleochronology, Phys. Rep. **208**, 267 (1991).

[58] T. Rauscher, F.-K. Thielemann and K.-L. Kratz, Nuclear level density and the determination of thermonuclear rates for astrophysics, Phys. Rev. C **56**, 1613 (1997).